


Article

Analytical Modeling and Control of Dual Active Bridge Converter Considering All Phase-Shifts [†]

Muhammad Faisal Fiaz ¹, Sandro Calligaro ^{1,*} , Mattia Iurich ² and Roberto Petrella ²

¹ Faculty of Science and Technology, Free University of Bozen-Bolzano, Piazza Università 5, 39100 Bolzano, Italy; muhammadfaisal.fiaz@natec.unibz.it

² Polytechnic Department of Engineering and Architecture, University of Udine, Via delle Scienze 206, 33100 Udine, UD, Italy; iurich.mattia@spes.uniud.it (M.I.); roberto.petrella@uniud.it (R.P.)

* Correspondence: sandro.calligaro@unibz.it

[†] This paper is an extended version of our paper published in 2020 IEEE Energy Conversion Congress and Exposition (ECCE), Detroit, MI, USA, 11–15 October 2020; Analytical Modelling and Control of Dual Active Bridge Converter Considering all Phase-Shifts.

Abstract: In the field of power electronics-based electrical power conversion, the Dual Active Bridge (DAB) topology has become very popular in recent years due to its characteristics (e.g., bidirectional operation and galvanic isolation), which are particularly suitable to applications such as interface to renewable energy sources, battery storage systems and in smart grids. Although this converter type has been extensively investigated, its analysis and control still pose many challenges, due to the multiple control variables that affect the complex behavior of the converter. This paper presents a theoretical model of the single-phase DAB converter. The proposed model is very general, i.e., it can consider any modulation technique and operating condition. In particular, the converter is seen as composed by four legs, each capable of generating voltage on the inductor, and by the two output legs, which can steer the resulting inductor current to the load. Three variables are considered as the control inputs, i.e., the phase-shifts with respect to one leg. This approach results in a very simple yet accurate closed-form algorithm for obtaining the inductor current waveform. Moreover, a novel analytical model is proposed for calculating the average output current, based on the phase-shift values, independently of the output voltage. It is also shown that average output current can be varied cycle-by-cycle, with no further dynamics. In fact, average output current is not affected by the initial value of inductor current or by DC offset (which may arise during transients). The proposed models can be exploited at several stages of development of a DAB: during the design stage, for fast iteration, when selecting its operating points and when designing the control. In fact, based on the analytical results, a novel control loop is proposed, which adopts a “fictitious” (i.e., open-loop) inner current regulation loop, which can be applied to any modulation scheme (e.g., Single Phase-Shift, Triple Phase-Shift, etc.). The main advantage of this control scheme is that the simple dynamics of the output voltage versus the average output current can be decoupled from the complicated relationship between the phase-shifts and the output current. Moreover, a Finite Control Set (FCS) method is proposed, which selects the optimal operating points for each operating condition and control request, ensuring full Zero-Voltage Switching (ZVS) in all cases. The analytical results obtained and control methods proposed are verified through simulations and extensive experimental tests.

Keywords: dual active bridge; zero voltage switching; phase-shift; average output current; inductor current



Citation: Fiaz, M.F.; Calligaro, S.; Iurich, M.; Petrella, R. Analytical Modeling and Control of Dual Active Bridge Converter Considering All Phase-Shifts. *Energies* **2022**, *15*, 2720. <https://doi.org/10.3390/en15082720>

Academic Editors: Miguel Castilla, Alberto Reatti and Salvatore Musumeci

Received: 5 January 2022

Accepted: 22 March 2022

Published: 7 April 2022

Publisher's Note: MDPI stays neutral with regard to jurisdictional claims in published maps and institutional affiliations.



Copyright: © 2022 by the authors. Licensee MDPI, Basel, Switzerland. This article is an open access article distributed under the terms and conditions of the Creative Commons Attribution (CC BY) license (<https://creativecommons.org/licenses/by/4.0/>).

1. Introduction

Due to several factors, including the increasing utilization of renewable energy and the trend towards electrification of mobility, there is a strong demand for electrical power conversion solutions for the interfacing between different systems, such as energy storage devices, renewable sources, local and wide grids and specific loads [1,2]. In this scenario,

bidirectional isolated DC-DC converters are attracting more and more attention due to their versatile applications [3,4]. Despite the strong commitment and investments in research by industry and academia, many challenges still exist, and many aspects would benefit even from small improvements in several aspects, especially efficiency, power density, reliability and cost. As in almost all applications of power electronics, there is a strong focus on efficiency, not only because of energy saving itself, but also because thermal power dissipation issues are crucial and ultimately significantly affect the cost and density of converters. Figure 1 depicts some of the applications of DC-DC converters.

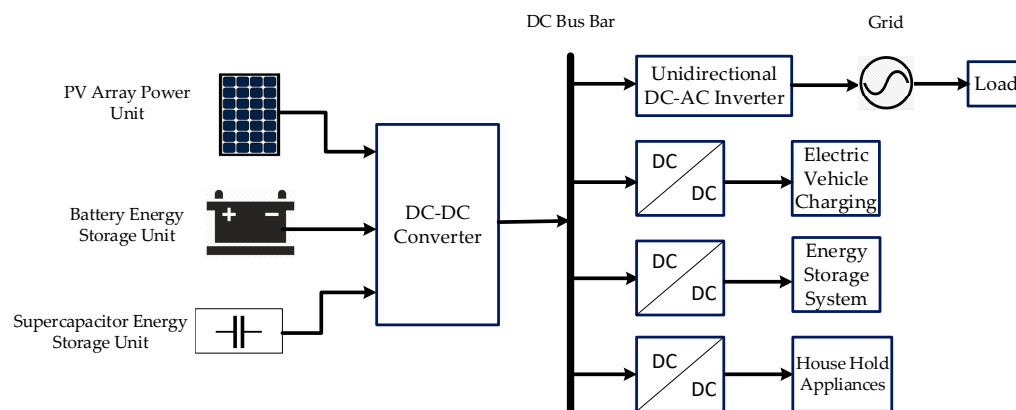


Figure 1. Applications example of DC-DC converters [5].

Among many applications, medium and large energy storage systems are expected to become very common applications in a few years, especially in the automotive market, given the growth trend of electric mobility. Converters operating as interfaces to batteries, for example, typically require isolation between input and output, operation across a wide range of input or output voltage and current, ensuring reliability, efficiency and controlled (smooth) operation. Vehicle-to-Grid (V2G) [6], i.e., the exchange of energy between electric/hybrid vehicles and the grid by means of the charging infrastructure, is also envisioned as a widespread application case of bidirectional converters operating as interfaces to batteries.

The DAB converter, first proposed in [7], is a popular choice as bidirectional DC-DC power converter. It consists of two active full-bridges, interfaced through a high-frequency transformer (Figure 2a), which allows the bidirectional power flow [8,9]. The topology, which is considered in this work, suits the requirements of the above-mentioned applications, e.g., bidirectional power flow, high-efficiency and wide conversion ratio capability. In fact, the single-phase DAB converter topology shows advantages with respect to other competing topologies [10–12] in terms of achievable converter efficiency, ease of bidirectional operation and controllability in general, modular structure and power density. Although this topology has been investigated quite extensively, the control of DAB still poses some challenges, due to the multiple control variables that affect the complex behavior of the converter [13–15]. Moreover, in the design of hardware and control there are several goals, e.g., regulating power flow in the two directions and in the whole range, achieving soft-switching (mainly Zero-Voltage Switching, ZVS) and minimizing the current stress of components [16–19].

In the analysis of the DAB, as for other converters, different points of view and abstraction levels need to be considered, e.g., the ideal behavior (steady state, dynamics), analysis of loss mechanisms, optimization of parameters and control [20–22]. Although simulation software can model parasitic effects of converters, sample-based simulations in the time domain (using iterative numerical solvers) may be too computationally intensive for the fast iteration of design and control choices [23]. In addition, an in-depth analysis of the converter's dynamic properties is required in order for the converter to work at a defined power level, in a desired power transfer direction, and to achieve high efficiency

over a wide operating range. Consequently, evaluating complex topologies necessitates a detailed analysis of the converter's response for a wide range of parameters, which can be time-consuming due to multiple iterations [24,25].

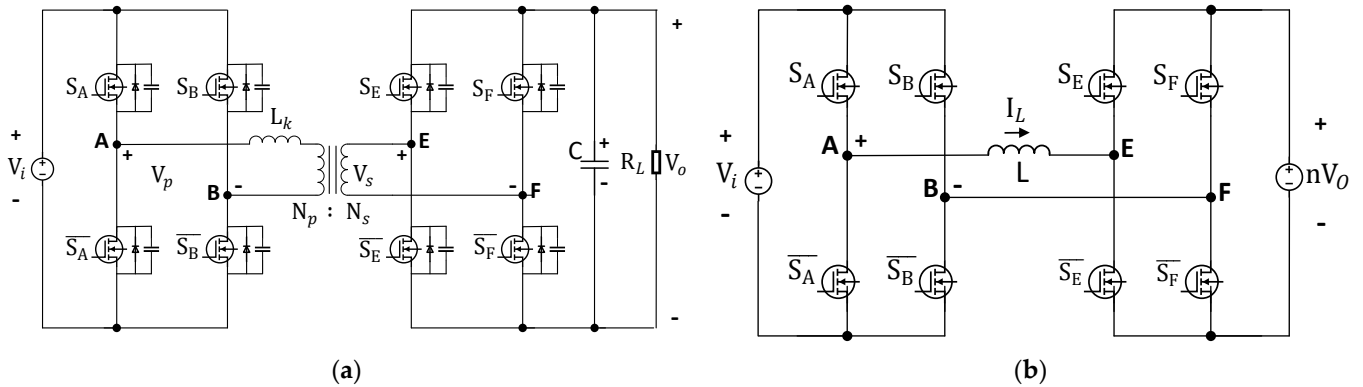


Figure 2. Dual Active Bridge DC-DC converter [7]: (a) Circuit diagram; (b) Simplified equivalent DAB circuit for inductor current behavior analysis.

Following this need, a theoretical model for the DAB converter is presented in [26], which is validated through extensive simulations and experimentally in this paper. The model, which considers ideal (non-dissipative) components, is very general, i.e., can be applied to any modulation technique. In fact, all the possible combinations of phase-shifts between the converter legs (i.e., all the “degrees of freedom” of the system) can be incorporated and studied with the same model. In the literature, the available mathematical models for the DAB are typically approximated [4,27] (e.g., only considering the first harmonic) or restricted to simple modulation modes [2,28], i.e., only one of the many possible phase-shift variations is considered. However, [29] proposes a superposition-based method for highlighting Zero Voltage Switching (ZVS) regions and AC terminal currents (peak and RMS) in DAB for all operating modes and modulation strategies. A similar approach has been independently developed by the authors of the present work, leading to similar results. Moreover, the study presented here extends the analysis, in particular regarding the response to control input variables in terms of output current of the converter, also considering the related dynamics. The proposed approach is applied to accurate modeling of the ideal behavior of DAB. Steady-state waveforms for any operating condition (i.e., any input and output voltage and combination of phase-shifts) are obtained in a very efficient way, using a so-called semi-analytical model. In addition, based on an original fully analytical model a control-oriented approach has been proposed in this paper. The model evaluates the average output current and results in a set of relatively simple equations. The presented novel full analytical modeling of the relationship between phase-shifts and average output current (at every switching period, i.e., “cycle-by-cycle”) becomes a valuable tool in the control development and design. By applying the proposed analysis to a classical modulation method (i.e., the Single Phase-Shift), the output current is fully characterized (analytically), obtaining a single formula for calculating the phase-shift value based on desired output current. This allows the cycle-by-cycle control of average current to be linearized, which makes voltage regulation very simple (similar to most other converters with inner current loop). As a study-case, SPS and proposed optimized control is used for regulating the output current (average) in an open-loop control (by linearizing the control of DAB output voltage). The proposed optimized control is based on FCS, where the control variables are chosen within a well-defined set of values, in this case a list of values for each phase-shift. With respect to previous work on the subject, many new figures have been included in this paper, together with the experimental section.

As an intermediate result, the presented analytical developments, based on the superposition principle, allow us to obtain the waveforms of the inductor and the output current

in closed form with a simple and fast procedure (“semi-analytical” model). This approach can therefore replace dynamic simulations, especially when the steady-state behavior is to be analyzed, with a much faster execution. This allows the application of optimization methods for the selection of the operating point or during the design phase (e.g., for the selection of inductance and frequency values). In addition, a novel, fully analytical model describes the relationship between output current and phase-shifts. The results obtained describe the average output current (at each switching period, i.e., “cycle-by-cycle”) as a function of input voltage and phase-shift values only, i.e., independently of output voltage. Such a model is very suitable for characterizing the dynamical behavior (e.g., for control purposes), since the converter can be considered a controlled (average) current source, as typically applied to with other converters.

Based on the analytical results, which link the desired output current to the corresponding phase-shifts, a novel control scheme is proposed, which uses a “fictitious” (i.e., open-loop) inner current controller. The main advantage of this method is that it can de-couple the simple dynamics of the output voltage versus the average output current (which is dominated by the output capacitor) from the complicated relationship between the phase-shifts and the output current. This control approach becomes straightforward in the case of SPS, but can be applied, indeed, to any other modulation technique. In fact, by leveraging the DAB behavioral model developed and mentioned above, an optimization procedure is set up, which results in the choice of optimal operating points, given input voltage and desired output average current. The proposed control approach considers a Finite Control Set, i.e., a certain number of combinations of phase-shift distributed over the whole range (between minimum and maximum phase-shift). The performance is evaluated and compared under both control methods, with variable output voltage. In addition, the analytical results obtained have been verified through simulations (using PLECS models) and experimentally.

In the next sections, the DAB is introduced first and then the analysis of its behavior at each switching period (cycle-by-cycle model) is presented. This study provides a closed-form method for describing the current waveforms of the converter, which is called “semi-analytical” model. The main usage of this model is to replace simulations, for fast iteration of design choices. Moreover, a fully analytical model is proposed, which describes the effect of control inputs (phase-shifts) on average output current, at each cycle. This result, which represents a novel contribution, is particularly interesting for design and implementation of the controller, since the converter can be considered as a controlled current source. It is worth highlighting that this model can take into account any combination of phase-shifts, i.e., is independent of the modulation technique adopted for the control of the converter. An example case is presented, on which the model is validated through simulation with PLECS Blockset in MATLAB/Simulink at the initial stage and finally verified through experiments, mainly considering the average output current at different operating points. The experiments on the proposed closed-loop SPS control with fictitious current control have been performed which show good agreement with theoretical results. Then, the tests with arbitrary (optimized) phase-shift triplets are performed, validating the proposed optimization method. Finally, by analyzing the converter performance, some interesting second-order effects (related to dead-times) are highlighted, which require further investigation.

2. Cycle-by-Cycle Model of DAB

The DAB topology consists of two full bridges (Figure 2a), namely “primary” and “secondary”, which are connected to each other by means of an isolation transformer. The transformer also introduces a suitable voltage ratio and (typically) the needed series inductance between the two bridges. Each of the four legs is typically controlled with 50% duty cycle, while the power flow is controlled by varying the phase-shifts of switch command signals. In the presented work, all the possible modulation schemes (i.e., any

phase-shift between any leg commands) are considered, to take advantage of any change in phase-shift to control the power flow.

The primary side bridge consists of legs A and B , with switches S_A , $\overline{S_A}$ and S_B , $\overline{S_B}$, while the secondary side bridge includes switches S_E , $\overline{S_E}$ and S_F , $\overline{S_F}$. All switching commands have a 50% duty cycle (complementary high and low sides), each leg has a phase value $(\varphi_A, \varphi_B, \varphi_E, \varphi_F)$, measured with respect to an arbitrary zero time-instant and normalized with respect to the switching period (i.e., a phase value of one corresponds to a delay of $1 - T_{SW}$). The primary-side bridge voltage (V_P) is generated with values $\pm V_i$ or zero, while the secondary-side voltage V_S is $\pm V_o$ or zero. The voltage across the leakage inductance (series inductance) L is the difference between V_P and the V_S reflected at the primary (i.e., nV_S), resulting in a current flow. The inductor current is usually controlled by changing the phase-shift between the primary and secondary commands (simplest modulation technique: single phase-shift [1,8,30]). The output current can be evaluated considering the state of the legs E and F , i.e., the inductor current (reflected to the secondary) is short-circuited (when $S_E = S_F$), directly routed to the output (when only S_E is on) or inverted (when only S_F is on).

The proposed theoretical approach for the analysis of DAB is based on modeling the inductor current by applying the superposition principle to account for the contribution of each bridge leg. A relatively similar approach was adopted for a limited number of cases in [30]. To simplify the analysis, some assumptions are made in advance: the losses are negligible, the four leg commands have the same frequency, and the voltage at the two sides of the converter ("input" and "output") is known and varies slowly (i.e., no voltage fluctuations occur within a switching period). These hypotheses are reasonable in terms of the waveform of the inductor current, while the losses can be considered as post processing. With the help of analytical calculations, a simple systematic closed-form method (hereafter referred to as the semi-analytical method) has been developed for calculating the inductor current waveform as the sum of the contributions from each transformer leg.

Since the phase-shift is a relative quantity, the command S_A is set for leg A with a phase-shift of zero. Thus, the independent variables (i.e., the "degrees of freedom" available as control inputs) are the phase-shifts of the remaining three switching commands, namely φ_B, φ_E and φ_F . The phase-shift values are variable and represent the time difference between two rising edges, normalized to the switching period (between -0.5 and $+0.5$). Assuming no losses (which, as mentioned above, is usually accepted at this level of abstraction), the inductor current is piecewise linear. For this reason, its waveform is represented entirely by the values at the switching points (i.e., the "vertices"), which are connected by straight-line segments. The approach considers a simplified double-bridge (primary and secondary inductor) circuit (Figure 2b) that exhibits bidirectional behavior. Each bridge consists of two legs with corresponding phase-shifts. An ideal transformer is assumed, i.e., the magnetizing inductance has been neglected, as is typically the case for DAB converters, while the leakage inductance is considered in the series inductor.

The magnitude and direction of the power flow or charge transfer at each switching cycle is determined by the respective phase-shifts between each leg and the reference one, i.e., leg A . Unlike previous work, in this case all possible modulation techniques can be considered, since the analysis is not constrained by any restriction between the four legs. Each bridge can connect the inductor and a DC voltage source (input or output), so that the square wave voltage sources of the primary and secondary bridges in Figure 3a have the same amplitude as the input voltage V_i (for V_A and V_B) or output voltage V_o (V_E and V_F).

According to the superposition principle, each leg acts on the inductor independently, so the analysis of inductor current waveform can be generally simplified. The total current flowing in the inductor is in fact the sum of contributions due to each leg:

$$i_L = i_{LA} - i_{LB} - i_{LE} + i_{LF} \quad (1)$$

Within each switching period, the switching times for each leg are given (taking into account the phase-shifts) and the current is calculated at these times (switching on and

switching off) of each leg, as shown in Figure 4. As you can see, the waveform of each component of the inductor current (i.e., for $i_{LA}, i_{LB}, i_{LE}, i_{LF}$) is very simple. In fact, the current is constant when the voltage is zero (i.e., before and after the same pulse), while it undergoes a linear variation during the voltage pulse. Thus, to determine the inductor current, one must distinguish between the instants within the pulse and the instants before or after the same pulse and calculate the slope of the current as follows:

$$\left. \frac{di_{L A,B}}{dt} \right|_{V_{A,F} \neq 0} = \frac{V_i}{L}, \quad \left. \frac{di_{L E,F}}{dt} \right|_{V_{B,E} \neq 0} = \frac{n V_o}{L} \quad (2)$$

The output current ($i_{o,avg}$) transferred to the load is calculated based on total inductor current and the switching state signals S_E, S_F of legs E, F , as shown in Figure 3b. The output current (i.e., flowing to the load and parallel output capacitor C) is then:

$$i_o = n \cdot i_L \cdot (S_E - S_F) \quad (3)$$

In this case, “output current” means the output of the secondary-side bridge to the output capacitor and load. The effect of possible (unwanted) DC current, which may be present at transients or due to non-ideal behavior, is also considered and using Equation (1), the total inductor current is:

$$i_L = i_{DC} + i_{LA} - i_{LB} - i_{LE} + i_{LF} \quad (4)$$

The average output current \bar{i}_o can be written as:

$$\bar{i}_o = \frac{n}{T_{sw}} \int_0^{T_{sw}} (i_{DC} + i_{LA} - i_{LB} - i_{LE} + i_{LF}) \cdot (S_E - S_F) dt \quad (5)$$

Based on (5), it is worth pointing out that the effect of DC inductor current on average output current is canceled out. In fact, while i_{DC} is a constant by definition, both S_E and S_F are 50% duty-cycle square-waves, which integral is equal and thus:

$$\frac{n}{T_{sw}} \int_0^{T_{sw}} i_{DC} \cdot (S_E - S_F) dt = \frac{n}{T_{sw}} i_{DC} \left(\int_0^{T_{sw}} S_E dt - \int_0^{T_{sw}} S_F dt \right) = 0 \quad (6)$$

Moreover, Equation (6) also shows that any change in the phase-shifts is reflected in variation of the average output current within the same switching period, i.e., no further dynamics is involved.

It is worth highlighting the importance of the results obtained above, in view of the converter control implementation. In fact, since the inductor current bias does not affect the average output current, it can be concluded that average output current does not depend on the initial value of inductor current (which is the only state variable in the circuit). For this reason, at each switching cycle, the output current is only due to phase-shift values and input voltage, with no effect from previous inputs. This means that output current (average) can be controlled in a strictly cycle-by-cycle fashion, which also defines the dynamics of current “actuation”. It is also worth to recall that average output current does not depend on output voltage (provided that the latter variation in a switching cycle is negligible), which clearly facilitates current control, allowing the converter to be considered as a controlled current source, which feeds the output capacitor and load, as done in many other converters.

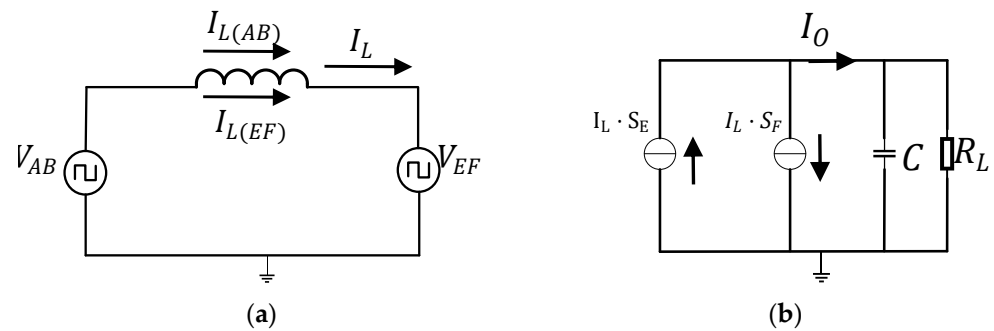


Figure 3. Inductor current decomposition: (a) equivalent circuit using to the superposition principle; (b) equivalent circuit for the analysis of average output current.

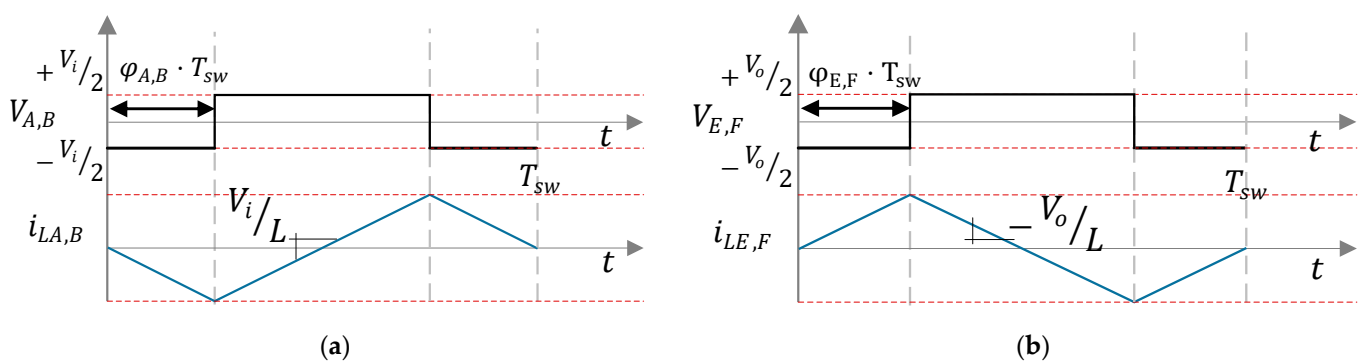


Figure 4. Gate signal and inductor current of each leg: (a) primary-side legs; (b) secondary-side legs.

2.1. Semi-Analytical Model

The superposition-based “semi-analytical” model is presented in this paragraph, which allows us to obtain the waveforms of inductor and output current, average output or input current, and of course, their peak values following a well-defined sequence of closed form steps. The RMS values of currents could also be calculated, given the simple shape of currents, which are piecewise linear.

However, this model is not condensed into a single set of equations that are able to determine the waveforms, but are expressed as a closed-form algorithm, hence the name “semi-analytical”. Consequently, currents in the converter are not described directly as analytical functions of time, but their values are calculated at breakpoints (i.e., at the switching instants of each leg), obtaining a full description of the waveform. The main quantity that is analyzed is obviously the main state variable of the converter within the switching period, i.e., the current flowing on the inductor, which has a piecewise-linear behavior, with switching events being its angle points.

Using the semi-analytical model, the evaluation of converter waveforms requires the following key steps:

- The generation of the set of switching instants within the period ($\varphi_x T_{sw}$ and $(\varphi_x + 0.5)T_{sw}$, in the correct order);
- Calculate the value of the inductor current caused by each leg at the switching instants (slope in Equation (2));
- Calculation of the total inductor current (Equation (1));
- Calculate the average of the output current as the area of the inductor current multiplied by $S_E - S_F$.

The procedure is analytical and has a closed form, but manual execution would be tedious. Therefore, the model was implemented as an algorithm (hence the name), with the parameters of the single-phase DAB (TIDA-010054) prototype given in Table 1. The procedure is analytical and is closed-form, but manual execution would be tedious, so the

model has been implemented as an algorithm (hence the name given), with the single-phase DAB (TIDA-010054) prototype parameters given in Table 1.

Table 1. DAB converter (TIDA-010054) specifications.

Parameter	Symbol	Value
Switching Frequency	f_{sw}	100 kHz
Switching Period	T_{sw}	10 μ s
Input Voltage	V_i	100
Output Voltage	V_o	variable
Transformer's Turns Ratio	$n = N_{pri}/N_{sec}$	1.6
Duty Cycle	d	50%
Inductance	L	36 μ H
Output Capacitor	C_{out}	300 μ F
Dead-time	T_{dt}	250 ns
SiC MOSFET Output Capacitance for Primary Side Switches	C_{oss_pri}	1.1 nF
SiC MOSFET Output Capacitance for Secondary Side Switches	C_{oss_sec}	0.6 nF
Turn on resistance (primary)	R_{dsON_pri}	16 m Ω
Turn on resistance (secondary)	R_{dsON_sec}	30 m Ω
Output resistor	R_{out}	22.8

2.2. Analytical Modeling of Average Output Current vs. Phase-Shifts

An original fully analytical model and control-oriented approach has been proposed in this section. The model evaluates the average output current and results in a set of equations. The presented novel full analytical modeling of the relationship between phase-shifts and average output current is foreseen as a valuable tool in the control development and design.

Expanding the expression (3) based on (1) leads to:

$$i_o = (i_{oEA} - i_{oEB} - i_{oEE} + i_{oEF}) - (i_{oFA} - i_{oFB} - i_{oFE} + i_{oFF}) \quad (7)$$

where $i_{o_{yx}}$ (with $y = E, F$ and $x = A, B, E, F$) represents the interaction between inductor current components (1) and E, F leg states (3):

$$i_{o_{yx}} = n \cdot i_{L_x} \cdot S_y \quad (8)$$

An analytical model for average output current (across the switching period, symbols with bar \bar{i}_o) is presented hereafter. The average is obviously the sum of the average of the components:

$$\begin{aligned} \bar{i}_o &= \frac{1}{T_{sw}} \int_{t-T_{sw}}^t i_o dt = (\bar{i}_{oEA} - \bar{i}_{oEB} - \bar{i}_{oEE} + \bar{i}_{oEF}) - (\bar{i}_{oFA} - \bar{i}_{oFB} - \bar{i}_{oFE} + \bar{i}_{oFF}) \\ &= \bar{i}_{oEA} - \bar{i}_{oEB} - \bar{i}_{oFA} + \bar{i}_{oFB} \end{aligned} \quad (9)$$

Some simplifications can be applied, since the terms $\bar{i}_{oEE}, \bar{i}_{oFF}$ and $\bar{i}_{oEF}, \bar{i}_{oFE}$, cancel each other. Two cases are considered (Figure 5) based on the value of:

$$\phi_{yx} = \phi_y - \phi_x \quad (10)$$

For each term, the peak inductor current variation (reflected to secondary) is:

$$\Delta I = +n \frac{1}{2} \frac{V_i}{L} \frac{T_{sw}}{4} \quad (11)$$

With small phase-shift ($0 \leq \phi_{yx} \leq \frac{1}{4}$), “positive” (triangle and trapezoid, $A_{O_{x^+}}$) and negative (triangle, $A_{O_{x^-}}$) areas are:

$$A_{O_{x^+}} = \Delta I T_{sw} \left(\frac{1}{8} + \phi_{yx} - 2\phi_{yx}^2 \right), \quad A_{O_{x^-}} = \Delta I T_{sw} \left(\frac{1}{8} - \phi_{yx} + 2\phi_{yx}^2 \right) \quad (12)$$

Therefore, the average output current is equal to:

$$\bar{i}_{o_{yx}} = \frac{A_{O_{x^+}} - A_{O_{x^-}}}{T_{sw}} = 2\Delta I (\phi_{yx} - 2\phi_{yx}^2) \quad (13)$$

When $\frac{1}{4} \leq \phi_{yx} \leq \frac{1}{2}$, the positive and negative integral contributions (area) are, in this case:

$$A_{O_{x^+}} = \Delta I T_{sw} \left(\frac{1}{8} + \phi_{yx} - 2\phi_{yx}^2 \right), \quad A_{O_{x^-}} = \Delta I T_{sw} \left(2\phi_{yx}^2 - \phi_{yx} + \frac{1}{8} \right) \quad (14)$$

Resulting in the following expression for the average output current:

$$\bar{i}_{o_{yx}} = \frac{A_{O_{x^+}} - A_{O_{x^-}}}{T_{sw}} = 2\Delta I (\phi_{yx} - 2\phi_{yx}^2) \quad (15)$$

Generalizing to include also the cases $-\frac{1}{4} \leq \phi_{yx} \leq 0$ and $-\frac{1}{2} \leq \phi_{yx} \leq -\frac{1}{4}$ average output current can be written as:

$$\bar{i}_{o_{yx}} = 2\Delta I (\phi_{yx} - \text{sign}(\phi_{yx}) 2\phi_{yx}^2) \quad (16)$$

Similar calculations could be developed for the input current, due to the symmetry of the two stages.

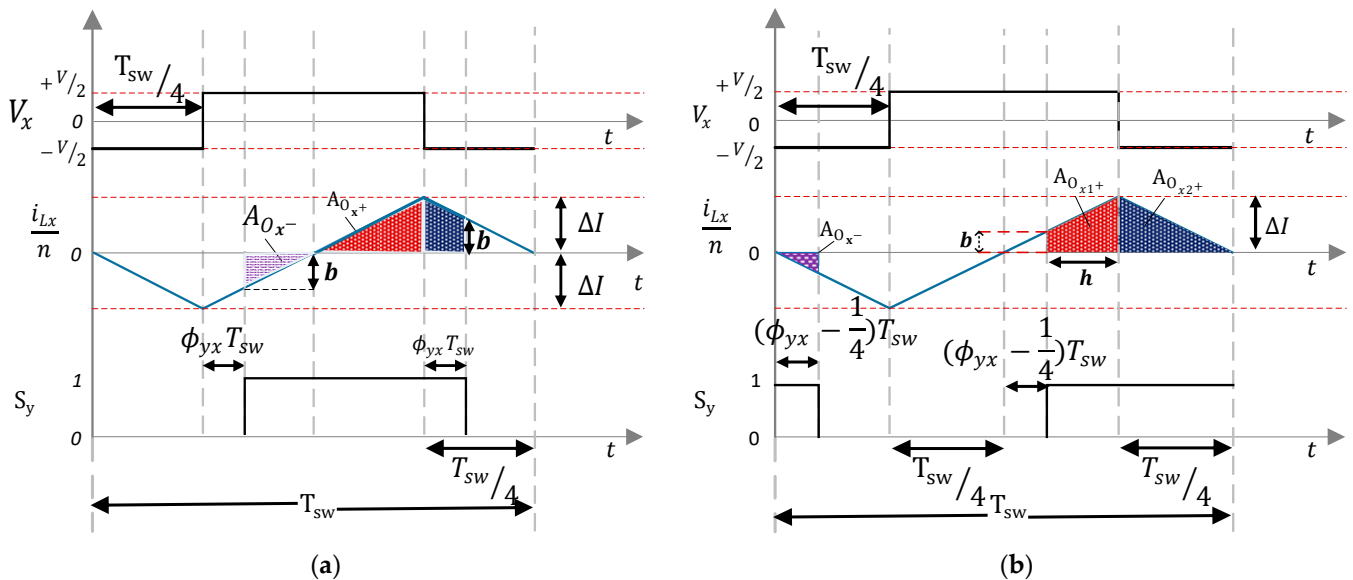


Figure 5. Contribution of one primary and secondary leg to the average output current: (a) Case 1; (b) Case 2.

3. Control Methods Based on the Cycle-by-Cycle Model

3.1. Operating Point Choice and Optimization

Usually, modulation has been performed using simple approaches, such as SPS [8,30]. However, the DAB modulation has three independent variables (i.e., three phase-shifts) or “degrees of freedom” that can be used as control variables. Indeed, thanks to the analytical

model presented above, it is possible to determine the effect of each of the phase-shift variables on the average output current. Moreover, the “semi-analytical” model, which can be run very quickly compared to numerical simulations, allows automatic optimization to improve the design decisions (mainly inductance, transformer ratio and switching frequency) and/or the converter operating point. In particular, the ability to evaluate any phase-shift between the four legs gives the designer complete freedom in finding the best modulation pattern. A reasonable goal for optimization would be to minimize conduction losses and current stress (in switches, inductor, and transformer) as well as switching losses (mainly related to the occurrence of ZVS) [27,31,32].

Typically, DAB control is aimed at regulating the output voltage. An accurate knowledge of the response with respect to the output current is very useful in this respect, since it practically determines the rate of change of the voltage across the output capacitor (C in Figures 2 and 3). If average output current can be imposed in a fast and accurate way, the classical structure with inner current control and outer voltage loop can be implemented, with obvious advantages in terms of tuning, stability and current limitation capability.

To control DAB at this level of abstraction, consider the following assumptions:

- The losses can be neglected (they are computed afterwards using the obtained waveforms);
- The four leg commands have the same frequency;
- The phase-shifts remain constant in each switching period;
- The “input voltage” (V_i) is known and varies slowly (i.e., negligible variation within a switching period);
- The variation of the “output voltage” (V_o) in a single switching period is negligible (this is a typical assumption that is practically true in steady state).

It is worth recalling (from the previous section) that any change in phase-shift is reflected in a corresponding change in the average output current within the same switching cycle, i.e., there is virtually no dynamic in the control of the current apart from the length of the switching period. Even though an offset may occur in the inductor current, e.g., during transients when the phase-shift is varied, the DC current does not affect the average output current (as shown in the previous analysis). Moreover, the average output current does not depend on the output voltage (V_o). This is particularly important for dynamic response and control, since the output voltage variations again depend on the average output current. Since the roles of input and output can be easily reversed (by simply considering $1/n$ as the transformer ratio instead of n), the constant voltage end (when one of the two is constant) can be called V_i for simplicity.

In the following paragraphs, the analytical results obtained by means of the cycle-by-cycle superposition-based analysis will be exploited, in order to propose two different control schematics for the voltage control of DAB, one using SPS modulation and one using a novel optimized modulation pattern.

3.2. Single Phase-Shift Control

As an application of the proposed approach to a classical modulation method (SPS), the output current is fully characterized (analytically), obtaining a single formula for calculating the phase-shift value based on desired output current. In principle, the proposed analytical approach could be easily extended to the case of a 3-phase DAB converter. The SPS case is considered in the following, where φ_E is the only control variable:

$$\varphi_A = 0, \quad \varphi_B = 0.5, \quad \varphi_F = \varphi_E + 0.5 \quad (17)$$

Using (13), considering the two cases for the sign of phase-shifts ϕ_{yx} , the average output current can be written as follows:

$$\bar{i}_o = 8\Delta I \times (\varphi_E - \text{sign}(\varphi_E)2\varphi_E^2) \quad (18)$$

For control purposes, this equation can be easily inverted to calculate the phase-shift value that results in the desired current, i.e.,

$$\varphi_E = \text{sign}(\bar{i}_o) \times \frac{1 - \sqrt{1 - \frac{|\bar{i}_o|}{\Delta I}}}{4} \tag{19}$$

By using this expression in the voltage controller, open-loop control of the average current is possible, allowing the implementation of a linearized voltage control, with the advantages of the typical nested current control loop as shown in Figure 6. Since the average output current is independent of output voltage, the inner “current control” is completely decoupled from the outer voltage loop, which simplifies the design of voltage regulator and ensures accurate current limitation and overall stability.

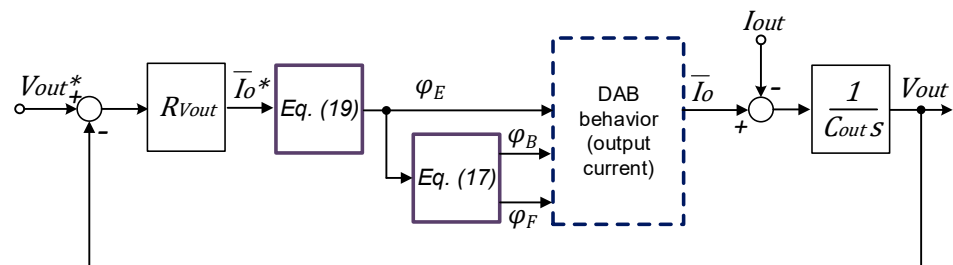


Figure 6. Control schematic for the SPS modulation.

3.3. Arbitrary Modulation (Optimized)

The proposed control approach (which involves an inner open-loop current control embedded in the closed-loop voltage control) can be generalized to be extended to any other modulation method. The schematic in Figure 7 shows a possible arrangement using Look Up Tables (LUTs) to obtain the three phase-shift values based on the desired output current. Instead of LUTs, of course, any other function could be used, e.g., analytical or empirical, even considering more than one input variable (e.g., selection could be based on input or output voltage values).

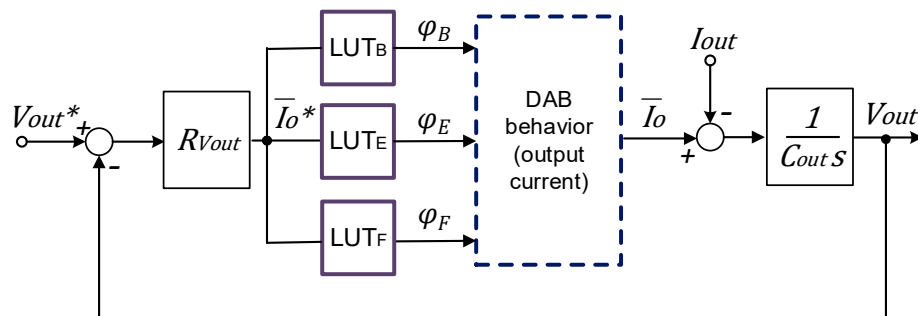


Figure 7. Control schematic for an arbitrary modulation (e.g., optimized).

Since, as mentioned above, the semi-analytical approach allows us to predict the behavior of the converter under many operating conditions with a reasonable computational effort, this can be used to optimize the operating point. In particular, the desired outcome in terms of control (desired output current) can be combined with other objectives (i.e., “multi-objective” optimization) by considering an appropriate cost function.

In the following, a cost function J has been formulated (20), which considers the current “control” accuracy, the current stress of the switches, conduction losses and occurrence of soft-switching. The function adopted is the sum of the squared average output current error $(I_o^* - \bar{i}_o)$, absolute maximum inductor current $\max\{|i_L|\}$ and zero voltage switching error ZVS_{error} . The latter variable evaluates the soft-switching capability in the specific

operating point is analyzed in terms of logical 1 for ZVS achieved in all legs and 0 otherwise along with ZVS_{error} which represents the amount of current missing before reaching the ZVS threshold. The constants W_{i_o} , W_{i_L} and W_{nZVS} are the weighting coefficients for the three parts of the cost, respectively:

$$J(\varphi_B, \varphi_E, \varphi_F, V_o, I_o^*) = W_{i_o}(I_o^* - \bar{i}_o)^2 + W_{i_L} \max\{|i_L|\} + W_{nZVS}(ZVS_{error}) \quad (20)$$

It is worth to mention that the cost function just introduced is only an example, which includes the most important aspects of the DAB operation. Different expressions can be proposed, also considering different variables, if there is a known relationship between each variable in the cost function and the independent variables, i.e., the phase-shifts, output voltage and desired output current.

In order to obtain the optimal modulation choice, a finite-set optimization is adopted in this case (according to the FCS approach). The whole range of phase-shift values (i.e., between -0.5 and $+0.5$), is evaluated, by considering many points in that range (in 0.005-sized steps). All the essential converter quantities are calculated for each phase-shift triplet (φ_B , φ_E and φ_F), using the semi-analytical model. Among the whole set of combinations, only those where ZVS is obtained in all legs are selected.

A large number of reference current values in the feasible range (i.e., within $\pm n \frac{1}{2} \frac{V_i}{L} \frac{T_{SW}}{4}$, spaced by 0.05 A) is considered for the cost calculation and the minimum-cost point among them is selected. The result of this finite-set optimization consists of three arrays (one for each phase-shift variable, i.e., φ_B , φ_E , φ_F), in which each value represents the minimum-cost operating point for a certain I_o^* value. The combination of current reference values and phase-shift values represents a LUT, which is used in the control schematic. The method can be extended for taking into account different values of output voltage, which is important especially in those cases where output voltage is variable across a wide range.

3.4. Comparison between SPS and Optimized Control with Variable Output Voltage

The evaluation of DAB behavior with variable V_o is done based on the parameters of single-phase DAB prototype parameters (see Table 1) from Texas Instruments (TIDA-010054). The detailed procedure for the comparison of SPS vs. optimized modulation is described in the following. Due to the differences between the two methods, two different procedures need to be implemented, although the final goal is the calculation of the cost function in the whole range of output current and voltage.

For the case of SPS modulation, the following steps are considered:

- Generating the set of V_o values ranging from 50 V to 150 V with the step of 10 V;
- Generating the set of average output current reference values ranging from $\pm \Delta I$ with the steps of 0.05 A for each V_o ;
- Setting up phase-shift values for SPS case (Equation (17));
- Calculating the value of φ_E by using Equation (19), for each reference average output current (desired current);
- Calculations of all the essential converter quantities are done for each phase-shift triplet (φ_B , φ_E and φ_F), using the semi-analytical model;
- Calculation of the total cost along with its components and saved in the relevant matrix for each average output current reference;
- All the cost components are evaluated and saved in their relevant matrices for each average output current reference;
- The procedure is carried out for each V_o value and the results are stored in 3 LUTs (matrices), one for each phase-shift (φ_B , φ_E and φ_F), representing optimal phase-shift choices as a function of the output voltage and desired output current.

For the case of optimized modulation, the evaluation procedure comprises the following steps:

- Generating the set of V_o values ranging from 50 V to 150 V with the step of 10 V;

- Evaluation of the finite control-set, i.e., the whole range of phase-shift values (i.e., between -0.5 and $+0.5$), by considering many points in that range (separated by small steps (0.005)) for each V_o ;
- Calculations of all the essential converter quantities are done for each phase-shift triplet (φ_B , φ_E and φ_F), using the semi-analytical model and saved in relevant matrices;
- Among the whole set of combinations, only those where ZVS is obtained in all legs are selected and the ZVS indexes are saved in relevant matrices;
- Generating the set of average output current reference values ranging from $\pm\Delta I$ with the steps of 0.05 A for each V_o ;
- Calculation of the total cost along with its components using the saved matrices;
- Minimum-cost points are selected within the subset of points that achieve ZVS from the total cost matrix for each average output current reference;
- All the other cost components are evaluated at minimum cost point index and saved in relevant matrices for each average output current reference;
- The procedure is carried out for each V_o value and the results are stored as 3D matrices.

The evaluation of DAB control with variable V_o is done for SPS and optimized modulation (according to the procedures described above), using the cost function J as the main comparison metric and analyzing its components. The ZVS range is also evaluated for both control methods. Each diagram in Figure 8 reports different components of the cost function, calculated for the two control options (SPS and optimal, "OPT"), together with the total cost (diagram (e)). The purpose of these figures is to quickly compare the effect of optimization, i.e., the minimization of peak current and the achievement of ZVS in the whole operating range (diagram (d)). (a) shows the average output current cost (i.e., control error) for SPS and optimized control. The output current cost for SPS control is practically zero as the phase-shift values are calculated using Equations (17) and (19), which gives the exact output current value. While in case of optimized control, the difference in average output current value is present (although small) and hence the cost is not null. The output current error (optimized control) is a consequence of the actual ZVS range, i.e., some current values cannot be obtained exactly, if ZVS is required. However, this does not seem to be a critical feature for the control, which is able to manage transient and steady-state operation even with discontinuities in the LUTs (since the control approach is FCS). The output current error also shows that in order to achieve ZVS, the low-current zone (which is visible because error increases linearly around zero, up to a certain point) must be practically avoided. Even if this is not a desirable condition, it can be accepted and, in the discontinuities, the control will operate similarly to a bang-bang control, with the advantage of preserving the ZVS condition, which is not met by SPS in the same range.

Figure 8b shows the peak current cost for SPS and optimized control, respectively. As shown in the diagrams, the peak current cost is relatively lower under optimized control than SPS control, especially at intermediate current values. This results in lower conduction losses for the converter and reduced stress on the components (in some cases, lower peak current could allow some downsizing of the active switch components). Similarly, (c) shows the ZVS cost for SPS and optimized control. The ZVS cost for optimized control is zero (since ZVS is always achieved), which makes it better than SPS control, in this regard. Practically, the LUTs that will be obtained are built discarding the points where ZVS is not possible. This means that the current control will not be accurate cycle-by-cycle, but can still be made accurate on average, i.e., on a longer period, according to the FCS control principle. Figure 8d shows the ZVS range for SPS and optimized control, in terms of logical 1 for ZVS achieved in all the legs or 0 otherwise. Under the optimized control, the wider ZVS range results in lower switching losses.

With optimized control scheme, ZVS is always obtained, and the peak inductor current is minimized. An important point is that the soft-switching range also depends on the value of leakage inductance and the switching frequency. The higher the value of the inductance, the more the soft-switching extends down to very low power levels (light loads). (e) shows

the total cost for SPS and optimized control, and the total cost of optimized control is less than SPS control, which results in reduced overall losses for the converter.

As already pointed out, the idea behind optimized control is to get rid of a rigid modulation, since each modulation starts from a certain idea or assumption, while in this case a wider range of possible combinations is explored (all “degrees of freedom”), in order to obtain ZVS and lowest current peak in the widest possible range. As can be seen from the 3D surfaces, this approach makes it possible to optimize the operation of the converter across the whole operating range, according to a certain cost function, in this case based on peak current and occurrence of soft-switching. Similar test can be done with other state of the art modulation techniques (i.e., Optimized control vs. EPS, DPS and TPS) to analyze the ZVS range and DAB performance.

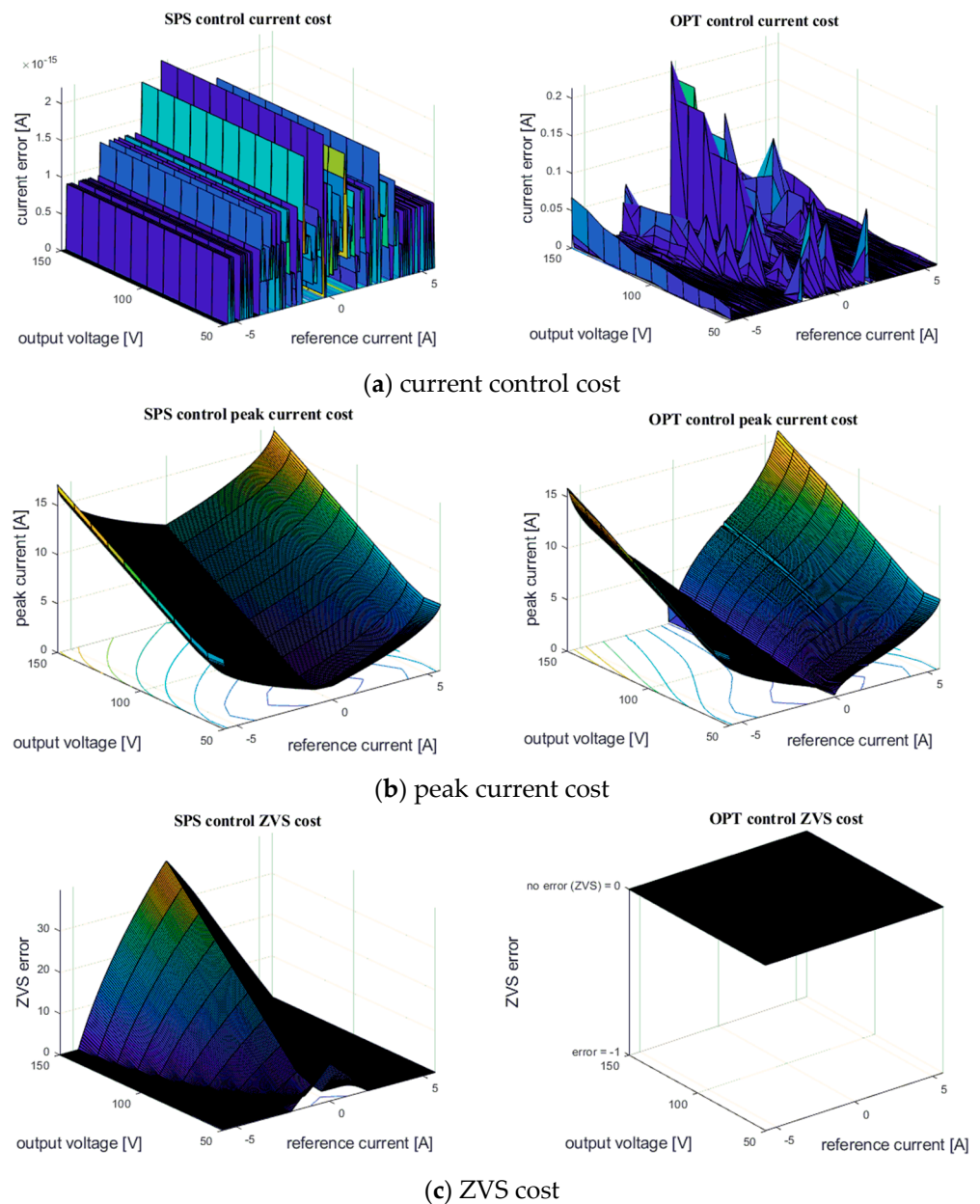


Figure 8. Cont.

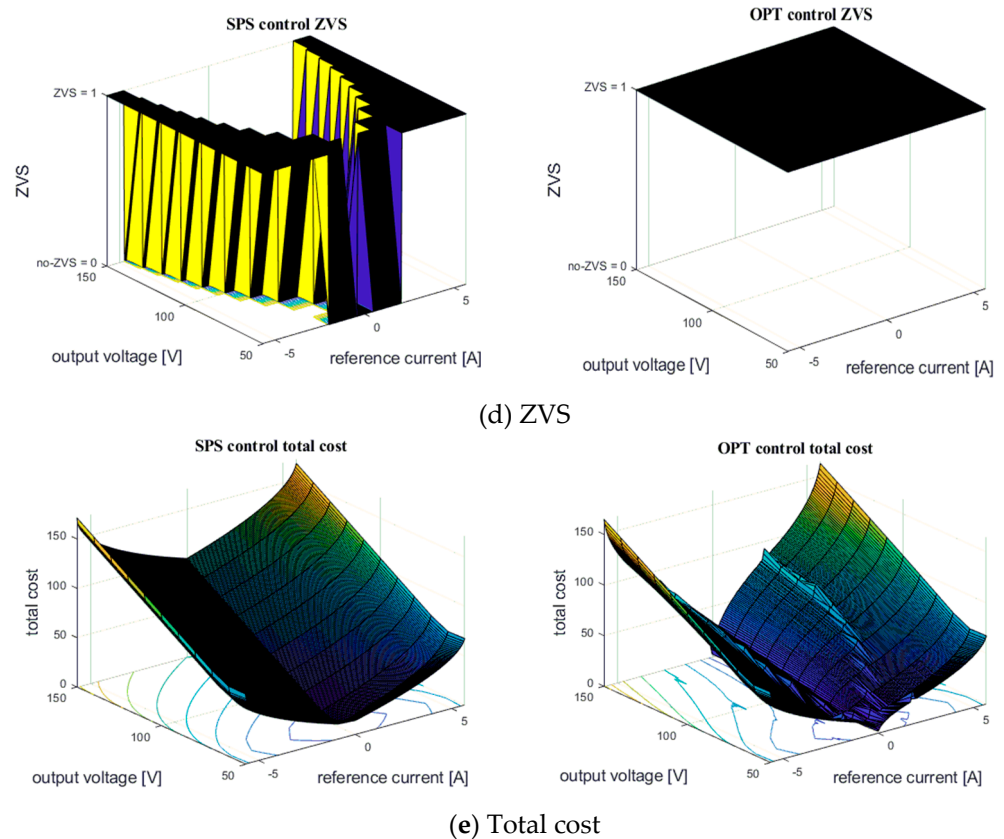


Figure 8. Cost function and its components, 3D surface plots for SPS control and optimized control, with variable voltage.

Moreover, optimization could be performed during the design of the converter, rather than for a specific hardware, to improve or select the design decisions (mainly inductance, transformer ratio, and switching frequency), the selection of the control method, and/or the performance of the converter. In particular, the ability to evaluate any phase-shift combination allows the search for the most appropriate modulation pattern.

4. Simulations

The DAB has been simulated using the Plexim PLECS blockset in MATLAB/Simulink environment, in order to validate the theoretical and analytical results. The circuit parameters are reported in Table 1. As a preliminary step, simulations of the ideal circuit (i.e., no lossy elements) at different phase-shift and output voltage values have been carried out, which confirm exactly the predictions from the analytical and semi-analytical models Table 2.

A second model has been built, which includes effects of parasitic capacitance and resistive effects, which emulate the losses in the real circuit [33]. The comparison between the average output current obtained by analytical model, PLECS simulation model (with losses) and the experimental model with different combinations of phase-shift values is reported and commented in the next section (Table 3). To validate the analytical results, simulation results for case 3 and case 5 are shown in Figure 9. Figure 10 shows the response to a change in the phase-shifts, occurring at 40 ms. The phase of leg E, φ_E is varied from the initial value of 0.25 to the final value of 0.30, while φ_B is 0.40 and $\varphi_F = -0.30$. Following the variation of φ_E , the average output current changes from 5.15 A to 4.75 A immediately (i.e., within one switching period), confirming that there is no real dynamics (except from the averaging operation applied) in the relationship between phase-shifts and average output current, i.e., the converter can be correctly modeled in a cycle-by-cycle fashion.

Table 2. Simulation of the ideal converter vs. analytical models: comparison of average output current with different combinations of phase-shift values.

Case	Phase-Shift Values			Average Output Current		
	φ_B	φ_E	φ_F	Semi-Analyt. Model	Analyt. Model	PLECS Sim.
1	0.50	0.25	0.75	5.55	5.55	5.55
2	0.50	0.10	0.60	3.55	3.55	3.55
3	0.50	0.35	0.85	4.66	4.66	4.66
4	0.20	0.10	0.30	1.33	1.33	1.33
5	0.40	0.25	0.65	5.11	5.11	5.11
6	0.45	0.15	0.75	5.22	5.22	5.22
7	0.50	0.06	0.56	2.48	2.48	2.48

Table 3. Comparison of average output current with different combinations of phase-shift values.

Case	Phase-Shift Values			Average Output Current (\bar{I}_o)				Efficiency (η)	
	φ_B	φ_E	φ_F	Analytical Model	Simulation	Experimental	Experimental Normalized	Simulation	Experimental
1	0.50	0.25	0.75	5.55	5.00	5.00	5.39	0.89	0.93
2	0.50	0.10	0.60	3.55	3.38	3.15	3.22	0.97	0.98
3	0.50	0.35	0.85	4.66	4.00	4.00	4.91	0.80	0.81
4	0.20	0.10	0.30	1.33	1.56	1.40	1.47	0.92	0.95
5	0.40	0.25	0.65	5.11	4.70	4.60	5.05	0.90	0.91
6	0.45	0.15	0.75	5.22	4.85	4.80	5.12	0.92	0.94
7	0.50	0.06	0.56	2.48	2.42	2.36	2.38	0.97	0.99

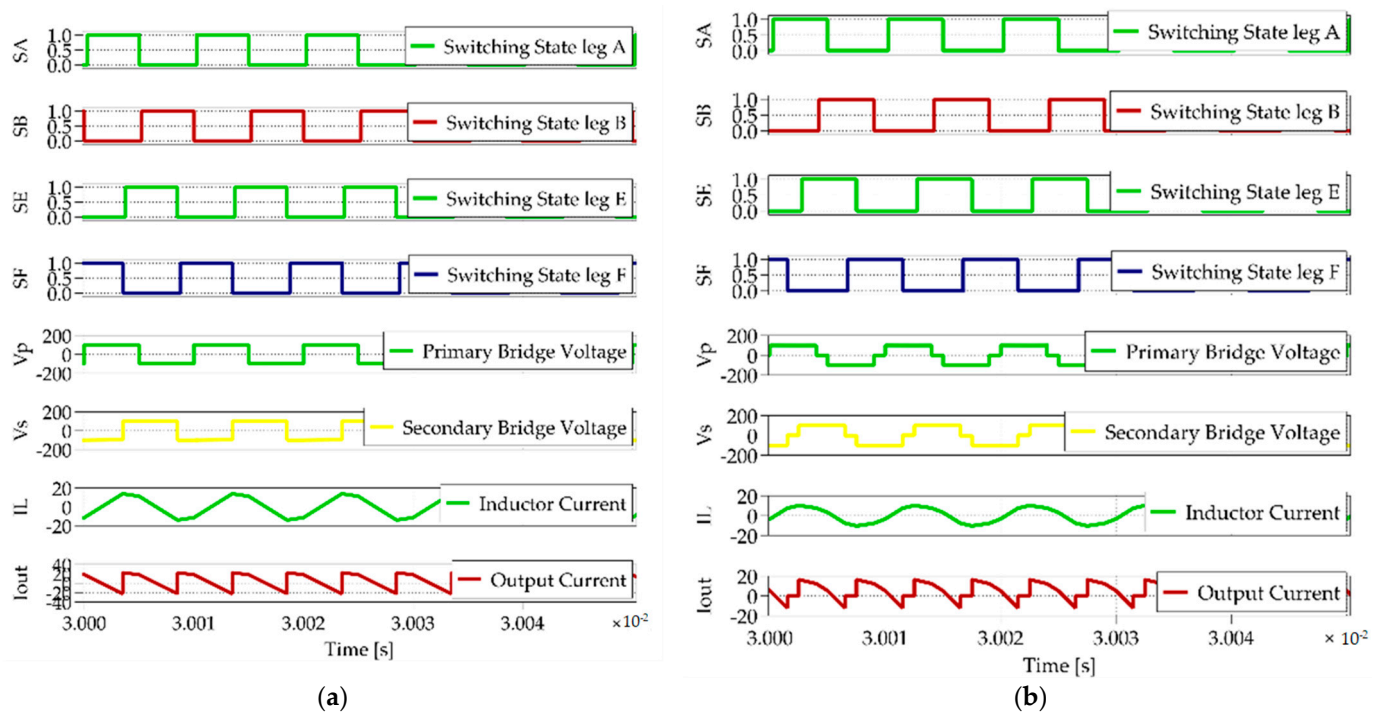


Figure 9. Gate control signals, primary and secondary voltage, inductor current and output current (PLECS simulation): (a) Case 3; (b) Case 5.

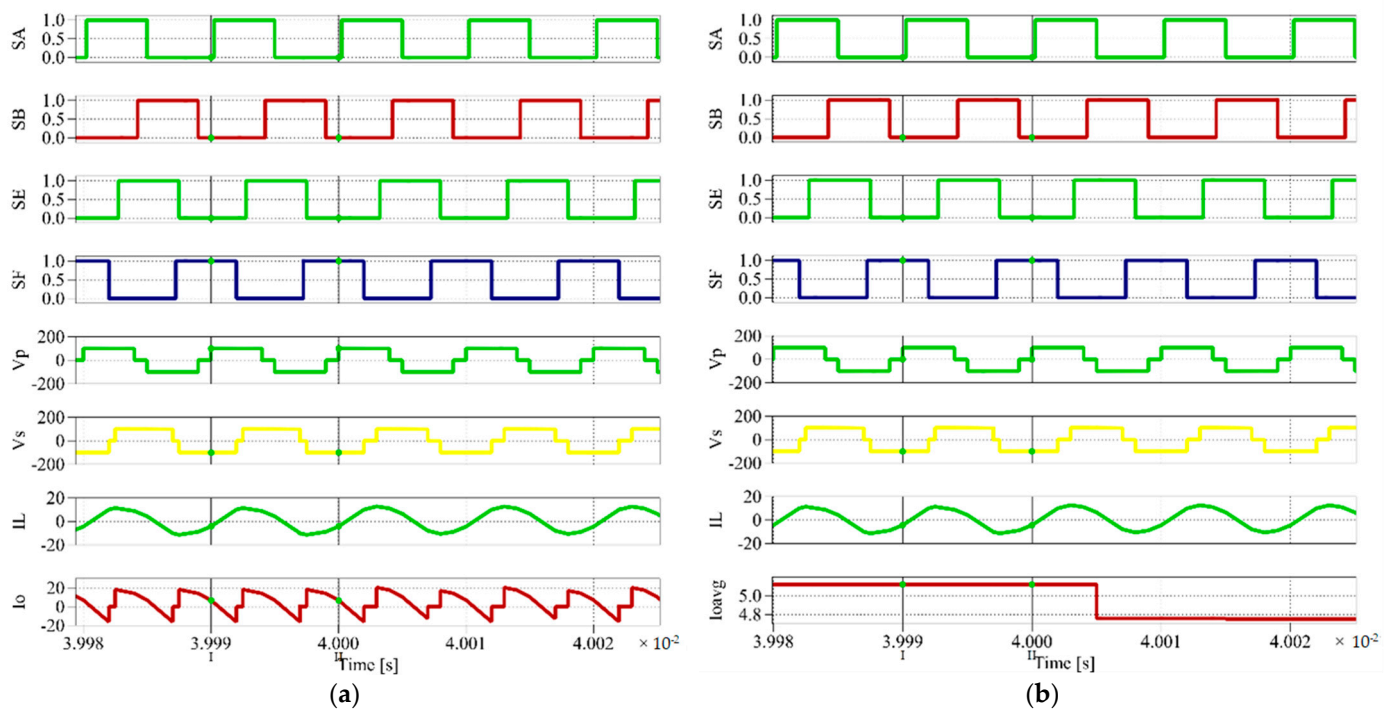


Figure 10. Gate control signals, primary and secondary voltage, inductor current and output current (step change, PLECS simulation): (a) Output current; (b) Average Output current.

The main waveforms over three periods for the phase-shift triplet case 1 using the semi-analytical method, PLECS blockset simulation and experimental model are shown in Figure 11 to demonstrate the inductor current matching. As you can see from the waveform, very good agreement is obtained between the three models. Many other cases have been successfully tested but are not shown due to space constraints. The control capability in the case of SPS modulation was also tested. Figure 12a shows the desired voltage, actual voltage, and low-pass output voltage in the top plot; $\varphi_B, \varphi_E, \varphi_F$ in the middle plot; the desired output current (i.e., the output of the voltage regulator) and the actual output current in the bottom plot. The proposed control strategy, which implements open-loop control of the average output current (based on analytical findings), provides the desired average output current and thus linearizes the dynamics of the voltage control, which simplifies the tuning of the voltage regulator. The converter is started with an output voltage of zero and an initial reference value of 100 V, which is gradually decreased by 15 V every 15 ms. The nested open-loop current control is demonstrated by matching between the reference and actual current.

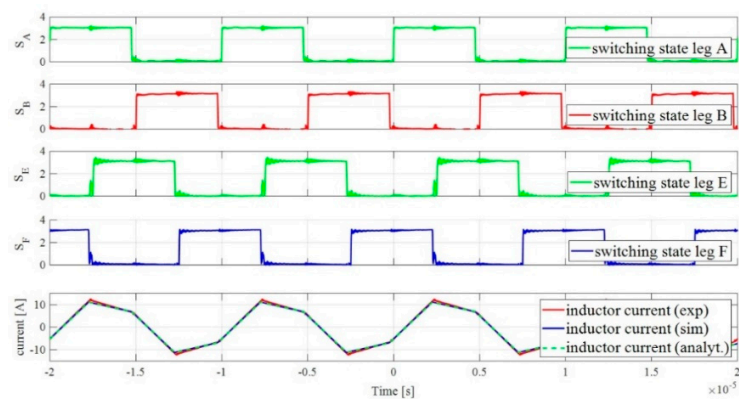


Figure 11. Gate control signals and inductor current matching waveforms for semi-analytical, PLECS simulation and experimental model (case 1).

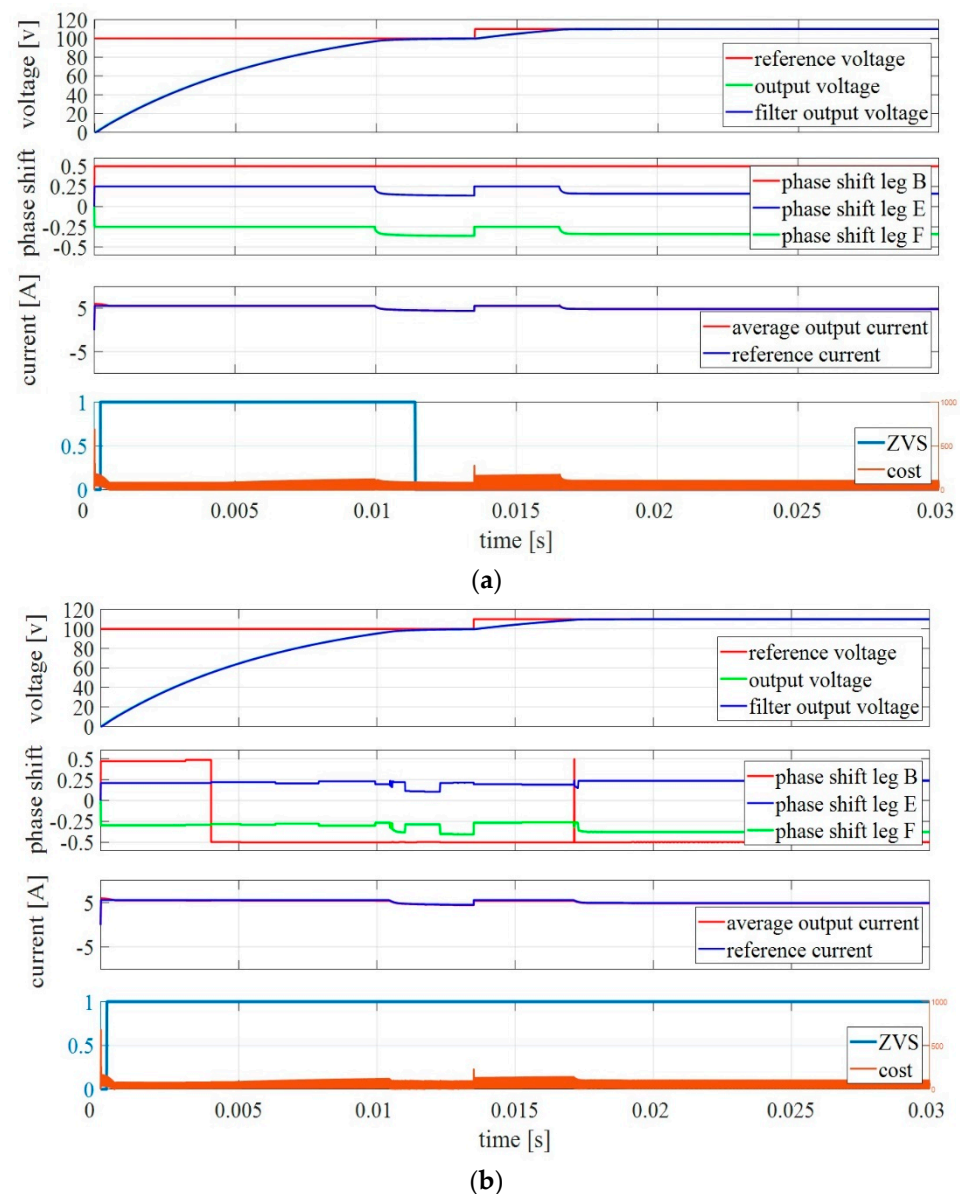


Figure 12. Output voltage control with startup from zero and step test (100 to 110 V): (a) SPS modulation; (b) Optimized modulation.

The simulation also confirms that any change in phase-shift affects the average output current (i.e., the charge transferred to the output), cycle by cycle and without delay. Although current control in a real converter becomes less accurate due to the non-ideal characteristics of the converter, the accuracy of voltage control remains almost unaffected thanks to feedback. A similar test (same conditions and reference voltage) is performed with any modulation method resulting from multi-objective optimization. The results of the test are given in Figure 12b. As can be seen, similar behavior is obtained in terms of control accuracy and dynamic range, which shows that the proposed control approach can be adapted to any modulation scheme, provided that the phase-shift values are correctly associated with the desired average output current. Moreover, the peak inductor current is minimized while the ZVS condition is preserved by the design of the controller. As mentioned before, the accuracy of the current control is not critical, which means that the accuracy can be traded with other characteristics such as efficiency or lower current load on the switches. In this case, at steady state, it can be observed that the output current ripple is reduced with respect to the SPS control, which in turn is related to the fact that the peak inductor current is minimized.

5. Experimental Results

The experimental work is presented to validate the obtained theoretical and PLECS simulation results and to check the correctness of the calculations, looking mainly at the average output current at different operating points (i.e., different phase-shift values). The experiments are performed on a prototype single-phase DAB (TIDA-010054), with key specifications shown in Table 1. The experimental setup and oscilloscope measuring the key waveforms of the DAB converter are shown in Figure 13.

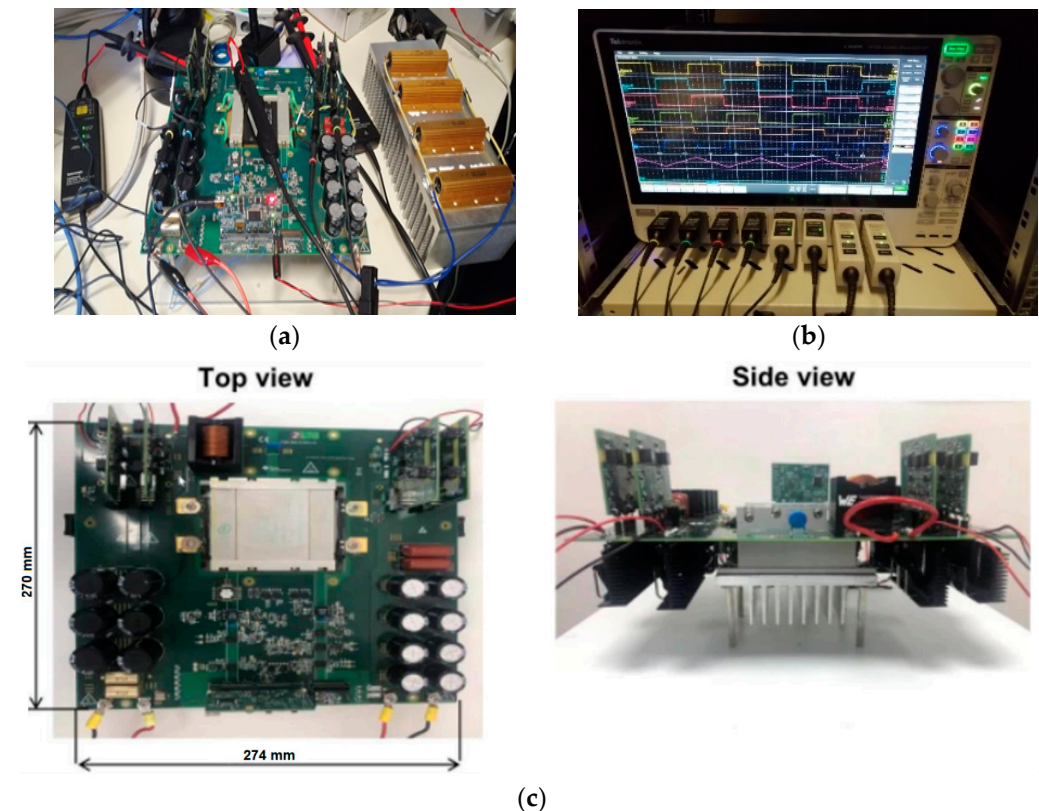


Figure 13. TIDA 010054 Board: (a) experimental setup; (b) oscilloscope measuring the key waveforms of the DAB converter; (c) top and side view.

5.1. Open-Loop Testing with Arbitrary Phase-Shifts

Open-loop tests with arbitrary phase-shift triplets are performed to validate and analyze the performance of the DAB DC-DC converter. All the tests are performed by using the DAB parameters shown in Table 1. First of all, for the sake of validation a few “random” triplets (φ_B = primary “negative” leg, φ_E = secondary “positive” leg and φ_F = secondary “negative” leg, see schematic) are chosen to compare the results. As the average output current is one of the novel findings of our work and it is independent of output voltage (only depends on input voltage and phase-shifts). In the calculations, the input voltage is kept to 100 V, so that it is simple to manage different values. The waveforms of important (inductor current, primary, secondary current and voltages, etc.) converter quantities are checked and recorded at the same operating points.

Table 3 shows the comparison between the average output current obtained by analytical model, PLECS simulation model and the experimental model with different combinations of phase-shift values. Average output current (experimental) as reported in the tables, is normalized by the experimental efficiency ($\bar{I}_{o_exp} / \eta_{exp}$) to match the analytical results to understand the effect of losses (switching and conduction mainly) on average output current [34–36]. The waveforms of the gate control signals, transformer’s primary and secondary voltage, inductor current and output current average of the experimental model (case 3 and case 5) are reported in Figure 14.

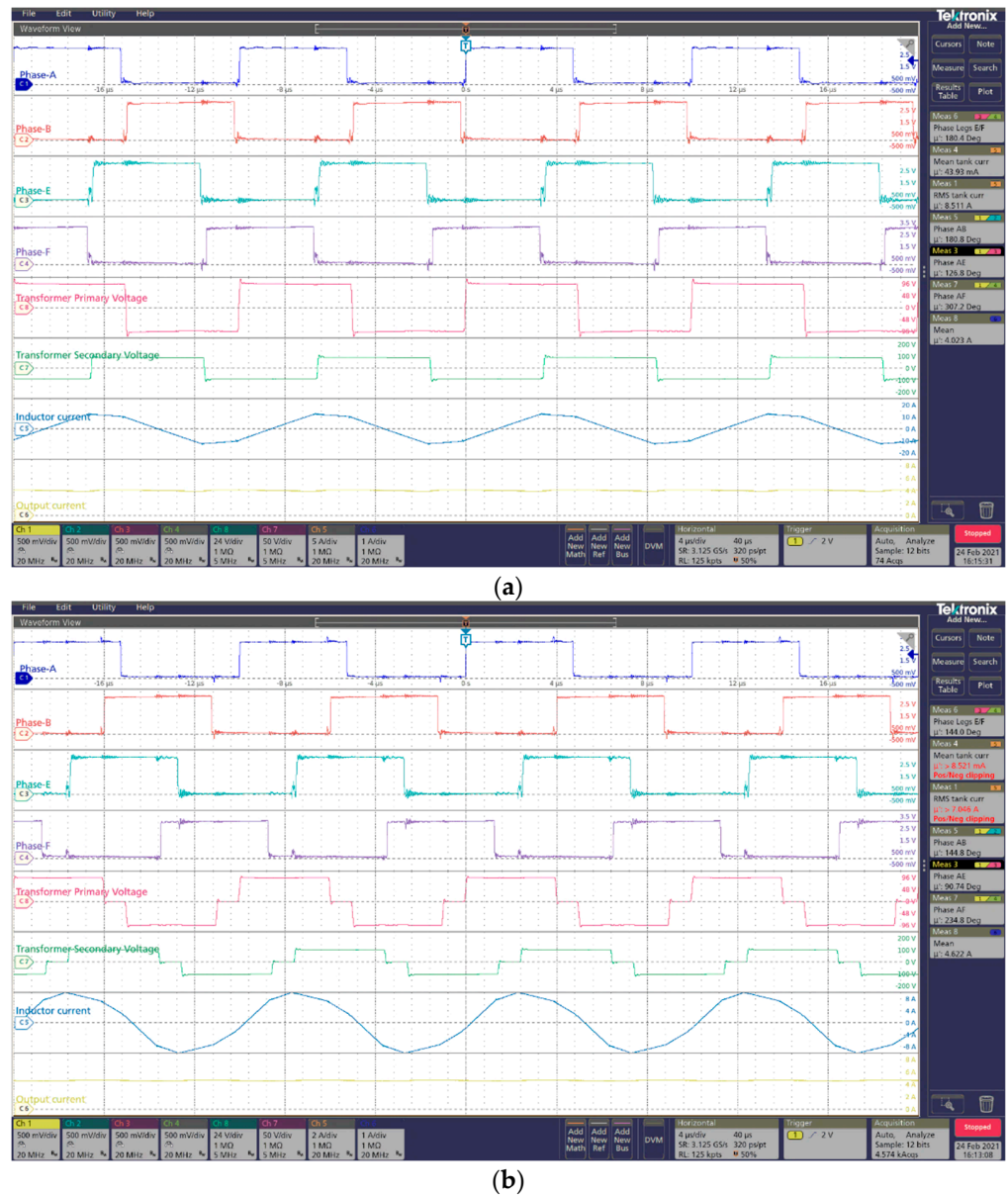


Figure 14. Gate control signals, transformer’s primary and secondary voltage, inductor current and output current average of the experimental model (open loop): (a) Case 3; (b) Case 5.

5.2. SPS Closed-Loop

Steady-state tests for SPS closed-loop control have been carried out with fixed input voltage (100 V) and different values of output voltage, which correspond to different values of phase-shift (φ_E). Varying the switching frequency between 60–140 kHz to analyze and optimize the ZVS threshold range, to figure out its effect on average output current and to exploit the switching frequency as a further degree of freedom to extend the ZVS range. These tests are performed as an application of the proposed SPS control method (presented in Section 3.1) and for the sake of experimental validation of the obtained analytical results with SPS closed-loop control.

The threshold current needed at each switching event (turn-on and turn-off) for each leg at primary and secondary side to ensure ZVS (i_{thr}) is figured out for each switching event as

$$i_{thr_pri} = \frac{2C_{oss_pri}V_i}{T_{dt}} \quad (21)$$

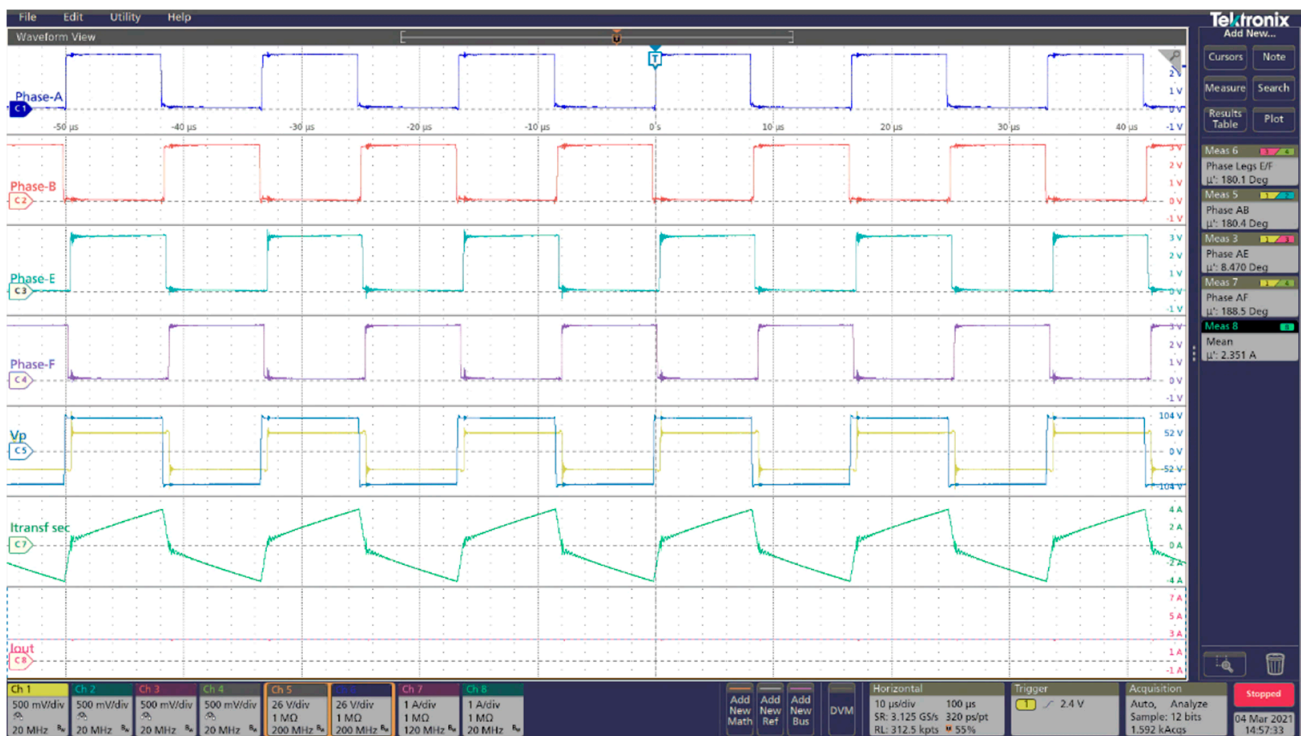
$$i_{thr_{sec}} = \frac{2C_{oss_sec}V_o}{T_{dt}} \quad (22)$$

The threshold current for each leg at primary side ($i_{thr_{pri}} = 0.88$ A) is constant as V_i is kept constant, while the $i_{thr_{sec}}$ is varied for each case as it depends on the output voltage. Table 4 shows the experimental results of the SPS closed-loop control tests at f_{sw} between 60–140 kHz, where reference current is normalized by the efficiency (i.e., $\bar{I}_o^* \cdot \eta_{exp}$) and error (normalized-measure) is the error between normalized reference current (\bar{I}_o^* norm) and the actual current (measured). It is assumed that the actual output voltage is equal to the reference voltage set by the software. Five cases have been reported for each test. Hard switching in the secondary switches is observed and reported in first two cases of each f_{sw} and from case no. 3 onwards soft-switching is achieved on both primary and secondary side, which is highlighted in green.

Table 4. SPS closed-loop test with variable switching frequency (60–140 kHz).

Switching Frequency	Case	Phase-Shift Value	Experimental (Measured)			Ref. \bar{I}_o^* Analytical	Normalized Ref. \bar{I}_o^*	Err. Normalized Measured
kHz	Case	φ_E	V_o	I_o	η_{exp}	\bar{I}_o^*	\bar{I}_o^* (norm)	%
60	1	0.020	52.00	2.28	0.96	1.48	1.42	−61.1
	2	0.022	53.40	2.34	0.97	1.58	1.53	−52.9
	3	0.033	54.85	2.41	0.97	2.32	2.25	−6.9
	4	0.035	55.00	2.41	0.98	2.38	2.32	−3.9
	5	0.046	62.00	2.72	0.97	3.14	3.06	11.1
80	1	0.029	51.00	2.24	0.96	1.53	1.47	−52.5
	2	0.031	52.00	2.28	0.96	1.61	1.55	−46.9
	3	0.047	53.40	2.34	0.97	2.35	2.28	−2.8
	4	0.051	55.00	2.41	0.98	2.56	2.50	3.4
	5	0.064	62.00	2.72	0.97	3.10	3.02	10.0
100	1	0.038	50.00	2.19	0.96	1.56	1.50	−46.2
	2	0.040	51.00	2.24	0.97	1.67	1.61	−38.6
	3	0.060	52.00	2.28	0.97	2.34	2.27	−0.26
	4	0.068	55.00	2.41	0.97	2.62	2.54	4.9
	5	0.083	62.00	2.72	0.97	3.06	2.96	8.3
120	1	0.030	40.00	1.75	0.91	1.05	0.95	−83.3
	2	0.052	49.80	2.19	0.97	1.74	1.68	−30.4
	3	0.070	50.00	2.20	0.96	2.23	2.15	−2.2
	4	0.075	51.00	2.50	1.08	2.38	2.57	2.8
	5	0.079	52.00	2.29	0.97	2.45	2.37	3.5
140	1	0.038	40.00	1.76	0.93	1.13	1.05	−68.1
	2	0.059	48.00	2.11	0.96	1.66	1.60	−31.8
	3	0.081	48.30	2.12	0.97	2.16	2.09	−1.6
	4	0.090	50.00	2.20	0.96	2.32	2.24	1.7
	5	0.093	51.00	2.24	0.97	2.40	2.32	3.6

Hard switching can be observed in the reported figures (case 2 of each test) in terms of noise/ringing in the key waveforms. There is not enough current present to discharge the secondary side MOSFETS output capacitors so in result V_{ds} is not zero at the turn on of leg E and F switches, which is causing the hard switching on the secondary side. It is also to be noted that the error between the measured and analytical average output current is relatively large only in the non-ZVS cases (which shows the effect of hard switching on output current), while it is relatively smaller in all the ZVS cases. In fact, a relatively large difference is observed in the φ_E value between ZVS and non-ZVS cases (between case no. 2 and 3 of each test). This is a known issue, related to the effect of dead-times, as pointed out in [37]. Figures 15–17 show the key waveforms and transition between ZVS and non-ZVS cases at 60, 100 and 140 kHz, respectively.



(a)

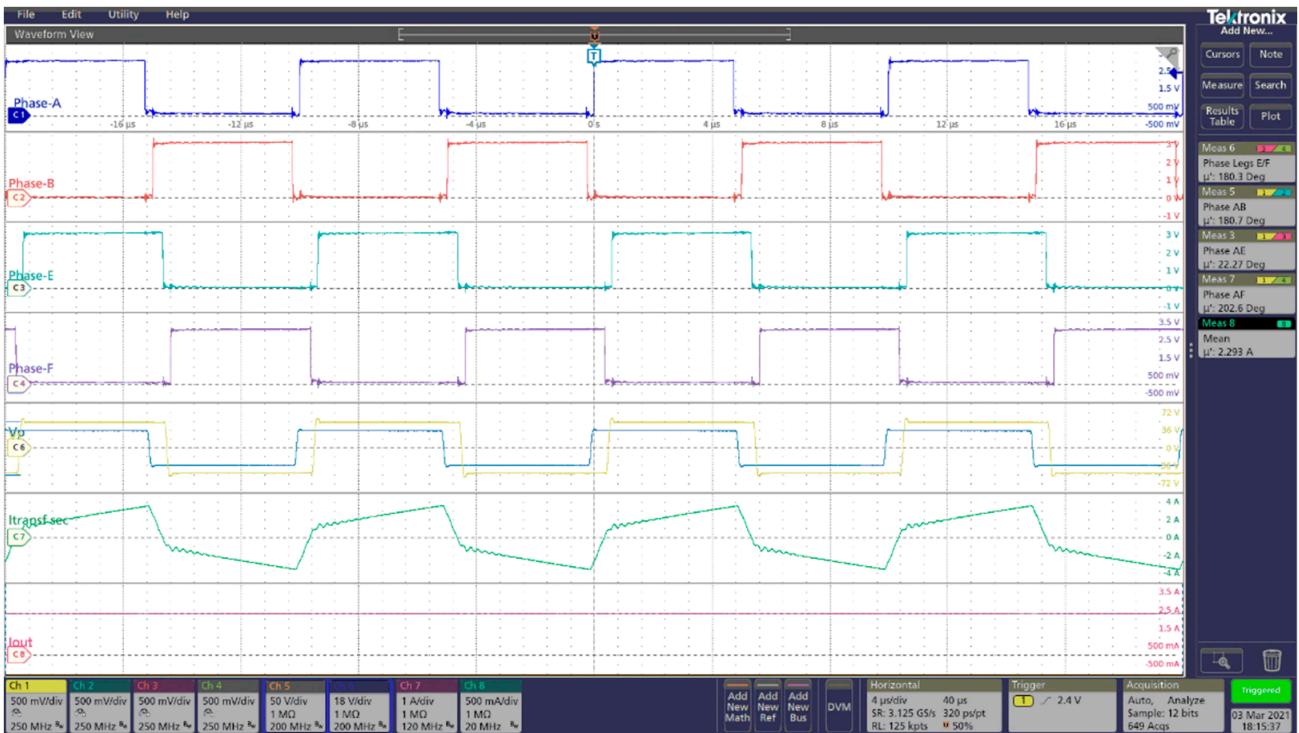


(b)

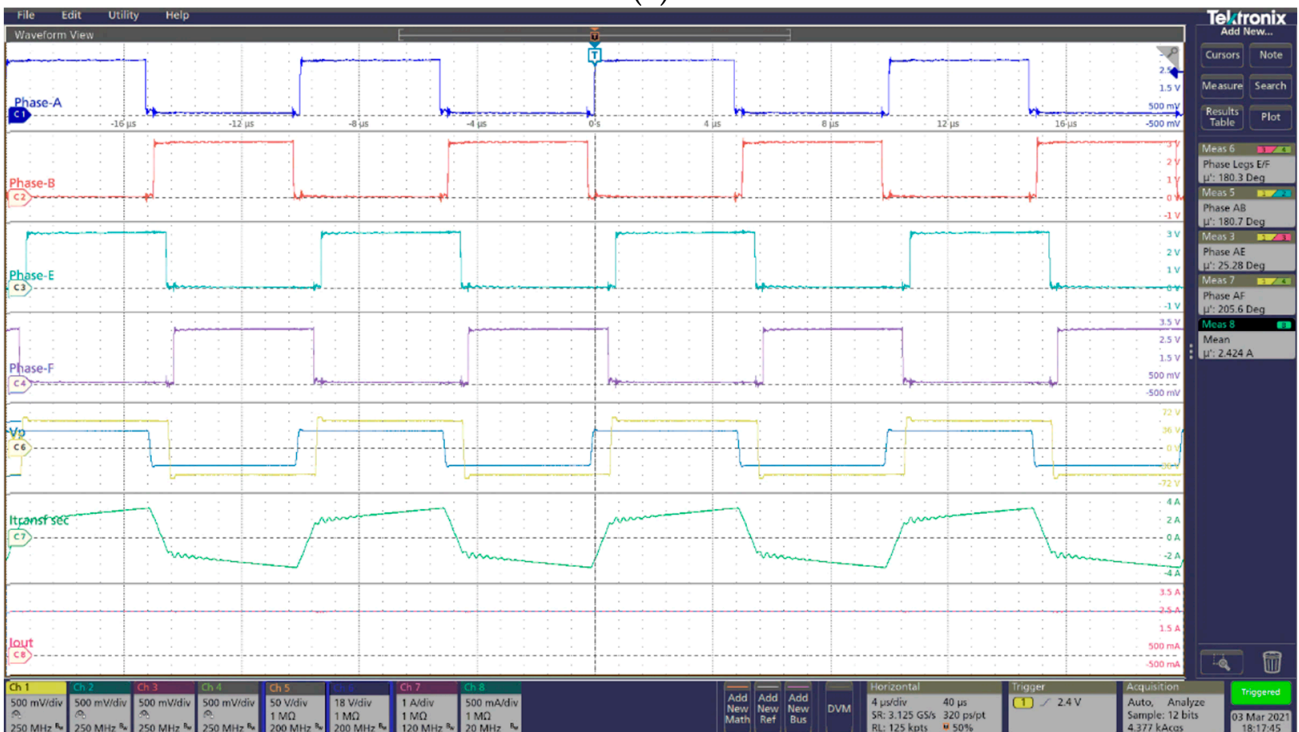
Figure 15. Gate control signals, transformer’s primary and secondary voltage, inductor current and output current average of the experimental model at 60 kHz: (a) Case 2; (b) Case 3.

Finally, the dynamical behavior of the proposed SPS closed-loop control scheme (Figure 6) has been tested, applying a step variation of the output voltage set point from 0 to 75 V. As shown in Figure 18, the experimental recording is almost overlapping the corresponding simulation trace. The rise time is consistent with the design of voltage regulator, which exploits the inner part of the schematic (open-loop current control) as a

controlled current source, which linearizes the behavior of the controller, as seen by the outer voltage regulation loop.

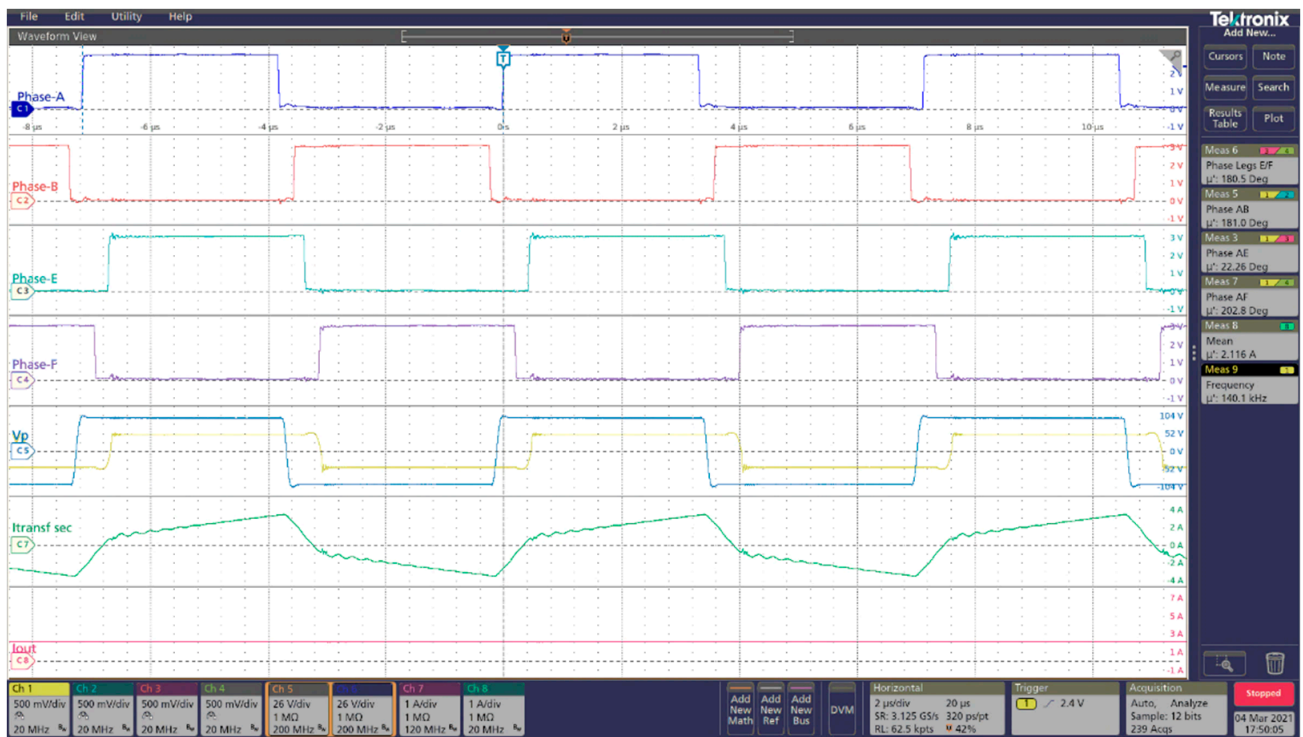


(a)

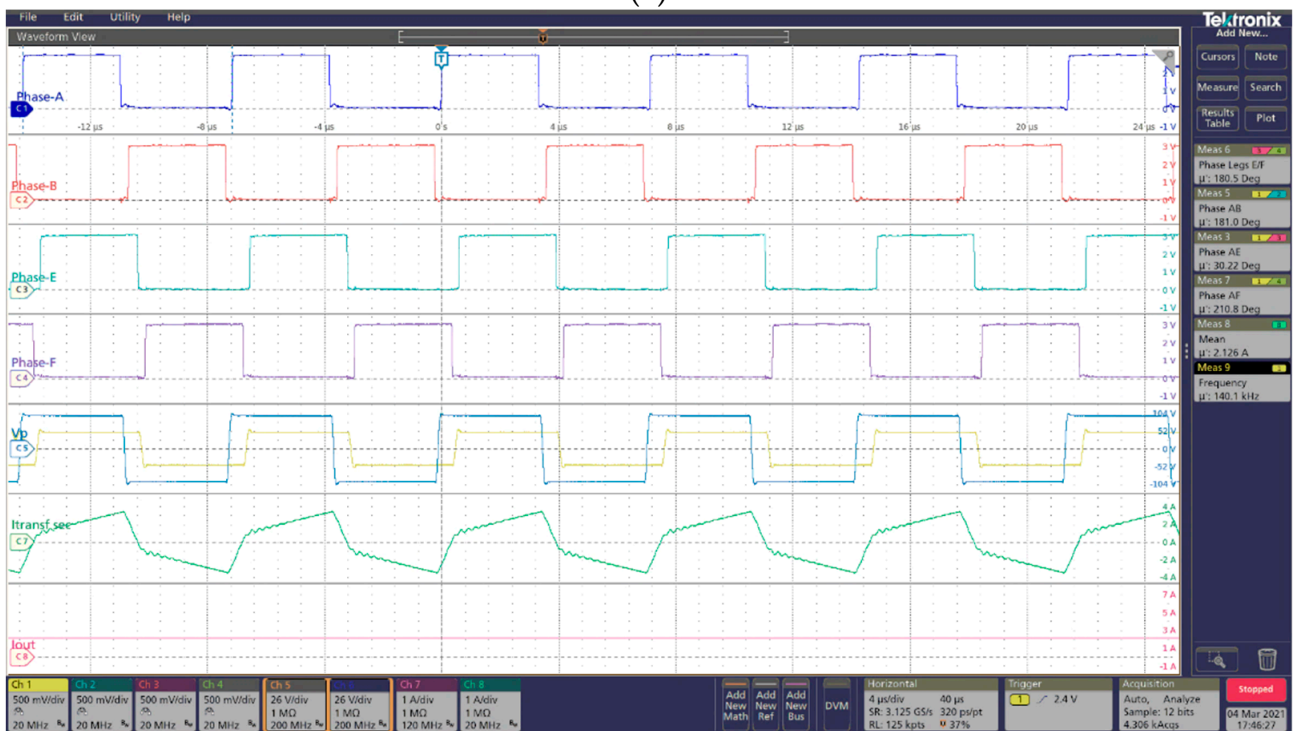


(b)

Figure 16. Gate control signals, transformer’s primary and secondary voltage, inductor current and output current average of the experimental model at 100 kHz: (a) Case 2; (b) Case 3.



(a)



(b)

Figure 17. Gate control signals, transformer’s primary and secondary voltage, inductor current and output current average of the experimental model at 140 kHz: (a) Case 2; (b) Case 3.

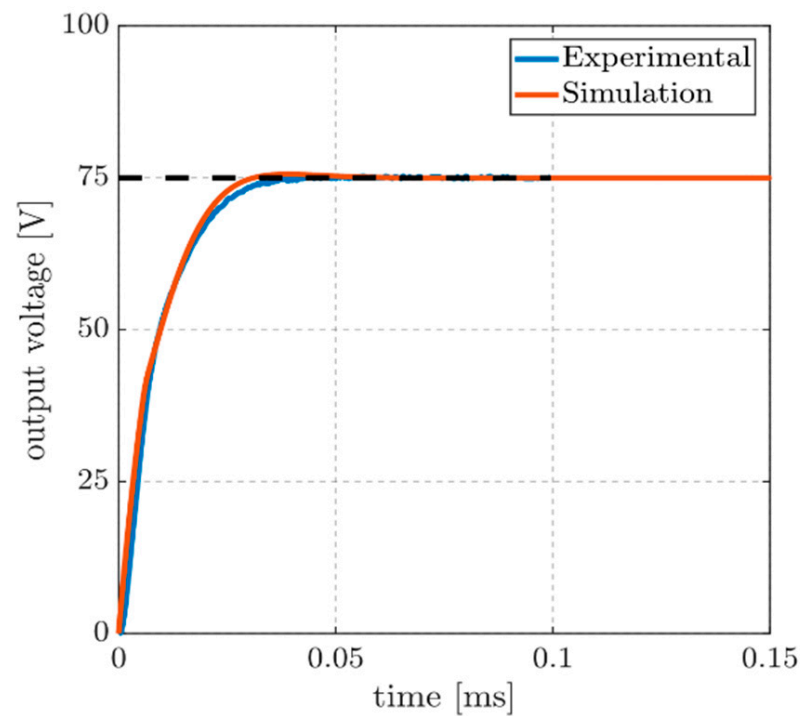


Figure 18. Step voltage response of the proposed SPS control, experimental vs. simulation.

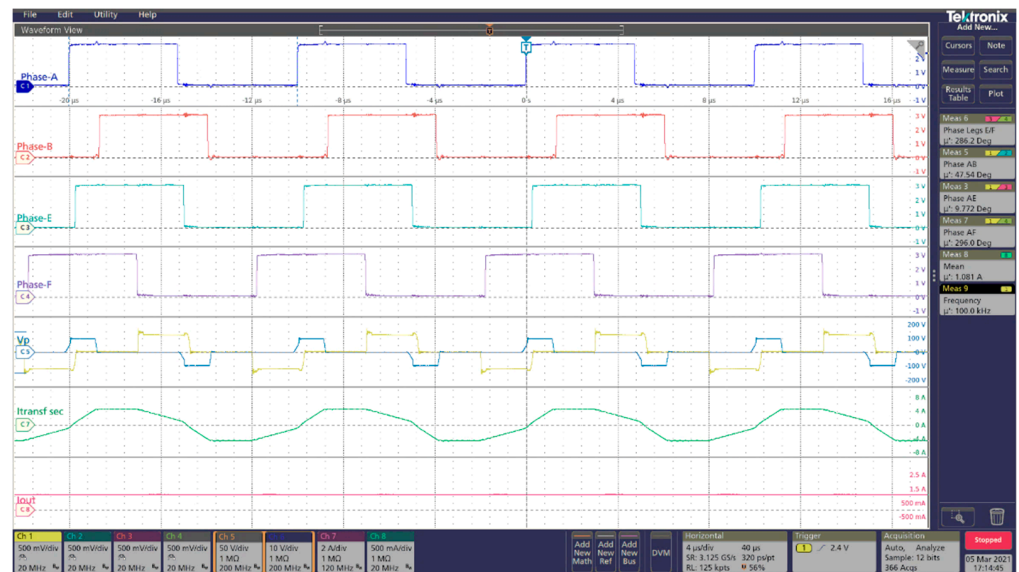
5.3. Open-Loop Optimized Control Testing

Open-loop optimized control test is done at 100 V input voltage and 100 kHz switching frequency. Since, as mentioned above, the semi-analytical approach allows us to predict the behavior of the converter under many operating conditions with a reasonable computational effort, this could be used to optimize the operating point. In particular, the desired outcome in terms of control (desired output current) can be combined with other objectives (i.e., “multi-objective” optimization) by considering an appropriate cost function. The tests are performed as an application of the proposed optimized control method presented in Section 3.2 and for the sake of experimental validation of the obtained analytical results with optimized control.

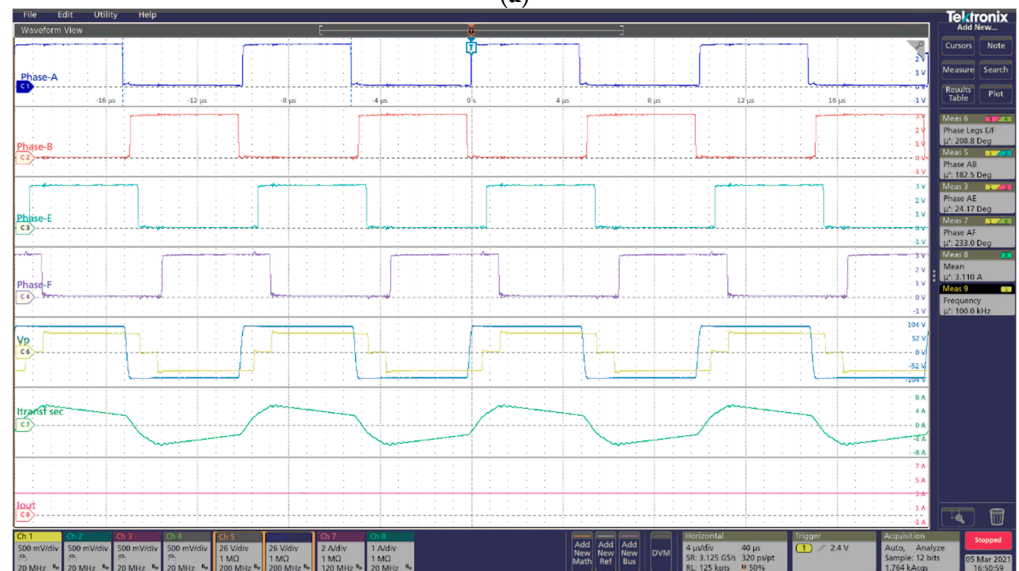
Table 5 shows the experimental results of the optimized open-loop control test at 100 kHz, where five cases have been reported. All the cases are with ZVS on primary and secondary side, since the optimization procedure only considers those phase-shift triplets where ZVS is obtained in all legs. Analytically optimized control results are verified, and quite good agreement is found between the analytical and experimental results. Figure 19 shows the key waveforms with minimum cost and ZVS on primary and secondary side switches.

Table 5. Optimized open loop control at 100 kHz.

Case	Phase-Shift Values			Experimental (Measured)			Ref. \bar{I}_o^* Analyt.	Normalized Ref. \bar{I}_o^*	Err. Normalized Measured
	φ_B	φ_E	φ_F	V_o	I_o	η_{exp}	\bar{I}_o^*	\bar{I}_o^* (Norm)	%
1	0.130	0.025	0.820	23.94	1.05	0.81	1.16	0.94	−11.95
2	0.445	0.030	0.530	50.16	2.20	0.94	2.19	2.07	−6.29
3	0.555	0.095	0.590	51.30	2.25	0.97	2.45	2.37	5.15
4	0.495	0.065	0.585	59.28	2.60	0.96	2.90	2.79	6.96
5	0.505	0.065	0.645	70.90	3.11	0.97	3.48	3.36	7.57



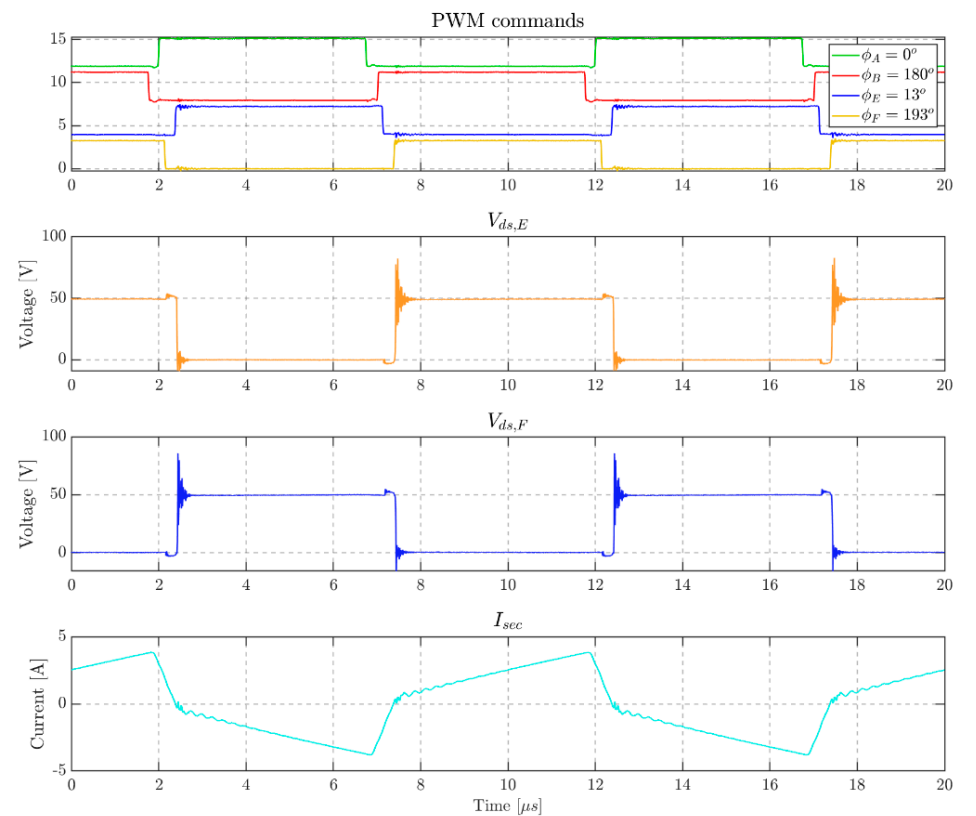
(a)



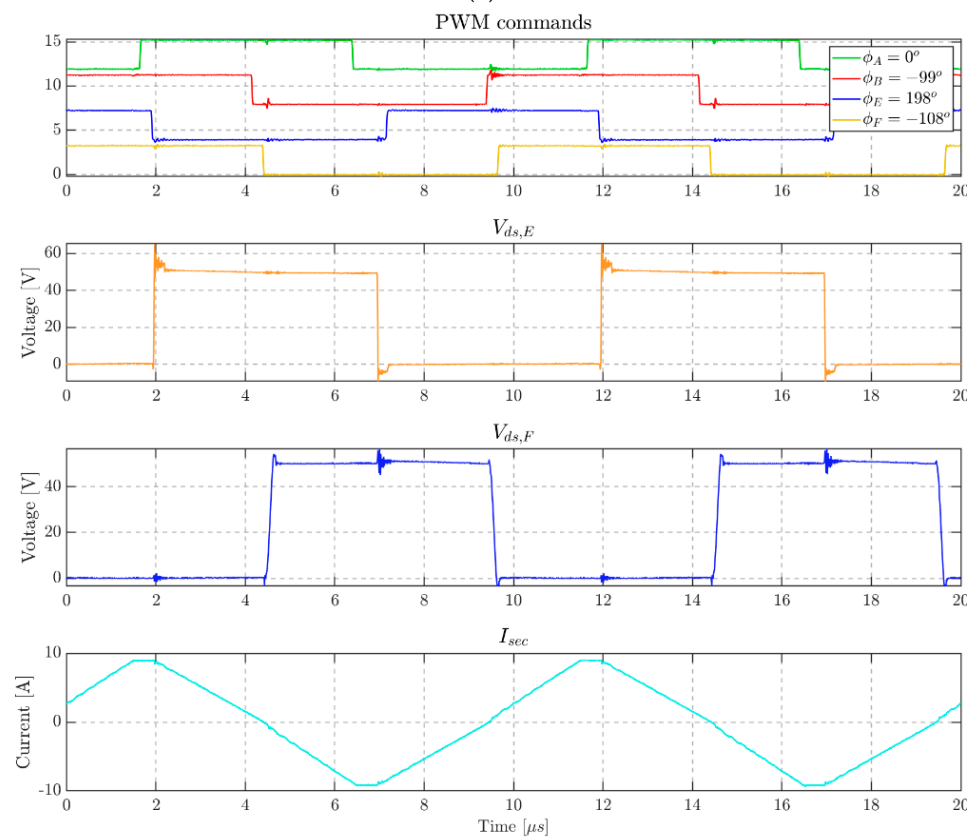
(b)

Figure 19. Gate control signals, transformer's primary and secondary voltage, inductor current and output current average of the experimental model at 100 kHz (optimized control): (a) Case 1; (b) Case 5.

In order to validate the optimized strategy, a comparison with the SPS has been carried out. The same operating condition has been set with both strategies, which is a reference output voltage of 50 V and 2.2 A as load current. In the SPS case shown in Figure 20a, the secondary legs (E and F) do not reach the ZVS condition. This is confirmed by looking at the 2nd (orange) and 3rd (blue) traces (high-side drain-to-source voltage of leg E and F, respectively) where a big ringing occurs during the turn-on of the active devices, indicating that they are in a hard-switching condition. Moreover, due to the voltage drop of diodes, the voltage during dead-times is either below zero or above output voltage. On the other hand, in Figure 20b, where the optimized modulation is shown, it can be seen how both legs E and F are in soft-switching state since the huge voltage ringing has disappeared, and it is clearly possible to observe the diode voltage drop (small overshoot on drain-to-source voltage as soon as the turn on ends).



(a)



(b)

Figure 20. Comparison between SPS control and optimized modulation; both the controls reach the same operating point: (a) SPS control, the secondary switches do not reach the ZVS condition; (b) arbitrary (optimized) control, all the legs reach the ZVS condition.

6. Comments on Experimental Results

This section presents some comments on the experimental work. The correctness of the calculations, looking mainly at the average output current at different operating points (i.e., different phase-shift values) is checked.

First, open-loop tests with arbitrary phase-shift triplets are performed, to validate and analyze the performance of the DAB DC-DC converter. The average output current results obtained by analytical model, PLECS simulation model and the experimental model in five different cases are compared. The PLECS simulation and experimental results match quite closely, considering that the simulation model includes the effects of parasitic capacitance and losses. A rather large discrepancy was found between analytical and experimental results, which was due to several stray losses present in the hardware [38–41]. Therefore, in this regards the efficiency plays a role in the power transfer and the converter efficiency is assumed to be unity in the analytical calculations. Hence, the average output current (experimental) is normalized by the estimated efficiency (I_{o_exp}/η_{exp}) to match the analytical results to understand the effect of losses (switching and conduction mainly) on average output current [42–45].

After that, closed-loop SPS control has been tested, in order to experimentally verify the implementation of the proposed SPS control schematic, which exploits the obtained analytical results. Closed-loop SPS tests are performed different values of the switching frequency. These tests show that the normalized error (based on efficiency) between the measured and analytical average output current is relatively large in the non-ZVS cases, while it is relatively smaller in all the ZVS cases. This is due to the different leg voltage that is obtained during the dead-time, depending on whether the switching occurs in ZVS or not. In some cases (namely, when the ZVS condition is not achieved), the output current cannot be simply considered a function of phase-shifts, since dead-times also play a relevant role [37,46,47], which should be further investigated. However, it is worth highlighting that the desired condition is ZVS, so this discrepancy can be avoided, by simply ensuring the desired (ZVS) condition is met (which is one of the features of the proposed optimized control).

It is worth highlighting that average output current and peak inductor current also depend on switching frequency. Therefore, it is expected that this variable should also be considered, in order to optimize the DAB operation, i.e., as a further degree of freedom. Including variable switching frequency in the optimization (e.g., by considering 2–3 different values) results in a relatively small increase of the computational cost.

The last test performed was the open loop optimized control test at 100 kHz switching frequency. Since the semi-analytical approach, as mentioned before, allows us to predict the behavior of the converter under many operating conditions with a reasonable computational effort, this can be used for the optimization of the operating point. In particular, the determined result in terms of control (desired output current) can be combined with other objectives (i.e., “multi-objective” optimization) by considering a suitable cost function. All the reported cases with optimized control exhibit the ZVS on primary and secondary side by design, since only the triplets achieving ZVS in all legs are considered in the optimization. Hence, the proposed analytical optimized control results are also verified experimentally.

7. Conclusions

This paper analyzes the behavior of DAB converter using an original approach, focusing on the relationship between control variables (i.e., phase-shifts) and output current. The analysis leads to two “cycle-by-cycle” models, which operate along one switching period. The first one is called “semi-analytical”, since it results in a closed-form algorithm, which gives all the converter waveforms as output. A fully analytical model has also been obtained, which predicts the average output current, depending on phase-shift values. Based on the analytical results, two different control schematics are proposed, one applying the well-known SPS modulation, while the other adopts optimal modulation patterns (i.e., combination of phase-shifts).

The semi-analytical method (i.e., a closed-form algorithm) can replace dynamic simulations (which are much more time-consuming and computationally intensive). The approach allows us to consider any modulation technique, i.e., no constraints are applied between the phases of the leg switching commands. As a result, a large number of different design parameter values and operating conditions can be tested, leading to more design iterations. Offline optimization of modulation selection (considering a certain cost function) has also been demonstrated, while online optimal control (e.g., for Model Predictive Control) is considered.

The fully analytical model evaluates the average output current as a function of phase-shifts, leading to a set of equations. The analysis performed in this work has shown that the relationship between the phase-shift values and the average output current does not depend on the output voltage and has virtually no dynamics (i.e., a variation in the phase-shift is reflected in the average output current within a single switching period, with no transient). By analyzing a classical modulation method (namely, single phase-shift) with the proposed method, the output current is fully (analytically) characterized as a function of a phase-shift value. Thus, the control problem can be solved by obtaining a single formula that gives the phase-shift value based on the desired output current. It is worth mentioning that, in principle, the proposed analytical approach can be easily extended to the case of a 3-phase converter DAB.

A voltage control scheme is then proposed and tested in simulation, where a “fictitious” (i.e., open) inner current control loop is implemented based on the analysis results linking the desired output current to the corresponding phase-shifts. The main advantage of this control scheme is that the simple dynamics of the output voltage versus the average output current (which is dominated by the output capacitor) can be decoupled from the complicated relationship between the phase-shifts and the output current. Indeed, the proposed control approach is more general since it can be applied to any modulation method (i.e., strategy to select an appropriate phase-shift triplet). This is demonstrated by applying an optimized modulation scheme as well as the SPS.

Given the relatively short execution time of the algorithm, many operating points can be explored offline. This allows for simple optimization of the converter or, as in this work, optimization of the operating point with respect to multiple objectives. In the present case, the ZVS constraint and the switch current load (i.e., peak inductor current) are considered along with the accuracy of controlling the average output current (open loop). The control method is very flexible and easy to implement (e.g., using LUTs), making it suitable for cost-sensitive applications.

The idea behind optimized control is to totally avoid rigid modulation rules, ensuring that all possibilities (i.e., all “degrees of freedom”) of the DAB converter are exploited, in order to obtain ZVS and lowest current peak in the widest possible range. SPS and optimized control with variable output voltage are analyzed to evaluate the DAB converter behavior using the cost function, along with its components. The ZVS range is also evaluated for both control methods. This approach makes it possible to optimize the operation of the converter across the whole operating range, according to a certain cost function, in this case based on peak current and occurrence of soft-switching. Moreover, the proposed approach could be used for various optimizations, such as selecting or improving the design decisions (mainly inductance, transformer ratio, and switching frequency), selecting the control method, and/or the converter performance. In particular, the ability to evaluate any phase-shift between the four legs gives the designer complete freedom in finding the most appropriate modulation pattern.

The validation of the models was performed by comparing the main steady-state waveforms and magnitudes of the converter obtained with different models (analytical, semi-analytical and dynamic simulation solver). The results confirm the investigated approach. The obtained analytical results are validated by simulations in PLECS Blockset and experimentally. The experiments on the proposed closed-loop SPS control with fictitious current control also show good agreement with theoretical results. Tests with arbitrary

(optimized) phase-shift triplets are also performed, validating the proposed optimization method and showing that the optimized modulation extends the ZVS range with respect to SPS. Finally, the SPS closed loop tests are also performed with variable switching frequency, which could be considered a further degree of freedom. In addition, by analyzing the converter performance, some interesting second-order effects (related to dead-times) were highlighted, which require further investigation.

Author Contributions: Conceptualization, M.F.F. and S.C.; validation, M.F.F. and M.I.; writing—original draft preparation, M.F.F. and S.C.; writing—review and editing, M.F.F., S.C., R.P.; supervision, R.P. All authors have read and agreed to the published version of the manuscript.

Funding: This research received no external funding.

Institutional Review Board Statement: Not applicable.

Informed Consent Statement: Not applicable.

Acknowledgments: The authors would like to thank the Free University of Bozen/Bolzano and the University of Udine for funding part of the work leading to this research article and the Texas Instruments Field Application Engineering service for providing materials used in experimental tests.

Conflicts of Interest: The authors declare no conflict of interest.

References

1. Rodríguez, A.; Vazquez, A.; Lamar, D.G.; Hernando, M.M.; Sebastian, J. Different purpose design strategies and techniques to improve the performance of a Dual Active Bridge with phase-shift control. *IEEE* **2014**, *30*, 790–804.
2. Rodríguez, A.; Sebastian, J.; Lamar, D.G.; Hernando, M.M.; Vazquez, A. An overall study of a dual active bridge for bidirectional DC/DC conversion. In Proceedings of the IEEE Energy Conversion Congress & Exposition (ECCE), Atlanta, GA, USA, 12–16 September 2010; pp. 1129–1135. [[CrossRef](#)]
3. Calderon, C.; Barrado, A.; Rodriguez, A.; Alou, P.; Lazaro, A.; Fernandez, C.; Zumel, P. General Analysis of Switching Modes in a Dual Active Bridge with Triple Phase Shift Modulation. *Energies* **2018**, *11*, 2419. [[CrossRef](#)]
4. Everts, J. *Modeling and Optimization of Bidirectional Dual Active Bridge AC–DC Converter Topologies*; KU Leuven: Heverlee, Belgium, 2014.
5. Tan, K.M.; Ramachandaramurthy, V.K.; Yong, J.Y. Integration of electric vehicles in smart grid: A review on vehicle to grid technologies and optimization techniques. *Renew. Sustain. Energy Rev.* **2016**, *53*, 720–732. [[CrossRef](#)]
6. Doncker, R.W.D.; Divan, D.M.; Kheraluwala, M.H. A three-phase soft-switched high-power-density DC/DC converter for high-power applications. *IEEE Trans. Ind. Appl.* **1988**, *27*, 796–805. Available online: <https://ieeexplore.ieee.org/abstract/document/67533> (accessed on 5 February 2018).
7. Zhao, B.; Song, Q.; Liu, W.; Sun, Y. Overview of Dual-Active-Bridge Isolated Bidirectional DC–DC Converter for High-Frequency-Link Power-Conversion System. *IEEE Trans. Power Electron.* **2013**, *29*, 4091–4106. [[CrossRef](#)]
8. Zhao, B.; Song, Q.; Liu, W. Power Characterization of Isolated Bidirectional Dual-Active-Bridge DC–DC Converter With Dual-Phase-Shift Control. *IEEE Trans. Power Electron.* **2012**, *27*, 4172–4176. [[CrossRef](#)]
9. Kim, M.; Rosekei, M.; Sul, S.-K.; De Doncker, R.W.A.A. A dual-phase-shift control strategy for dual-active-bridge DC-DC converter in wide voltage range. In Proceedings of the 8th International Conference on Power Electronics—ECCE Asia, Jeju, Korea, 29 May–2 June 2011; pp. 364–371.
10. Xue, L.-K.; Wang, P.; Wang, Y.-F.; Bei, T.-Z.; Yan, H.-Y. A Four-Phase High Voltage Conversion Ratio Bidirectional DC-DC Converter for Battery Applications. *Energies* **2015**, *8*, 6399–6426. [[CrossRef](#)]
11. Ibrahim, O.; Yahaya, N.Z.; Saad, N.; Ahmed, K.Y. Design and simulation of phase-shifted full bridge converter for hybrid energy systems. In Proceedings of the 6th International Conference on Intelligent and Advanced Systems (ICIAS), Kuala Lumpur, Malaysia, 15–17 August 2016; pp. 1–6. [[CrossRef](#)]
12. Azab, M.; Serrano-Fontova, A. Optimal Tuning of Fractional Order Controllers for Dual Active Bridge-Based DC Microgrid Including Voltage Stability Assessment. *Electronics* **2021**, *10*, 1109. [[CrossRef](#)]
13. Herrera-Jaramillo, D.; Henao-Bravo, E.; Montoya, D.G.; Ramos-Paja, C.; Saavedra-Montes, A. Control-Oriented Model of Photovoltaic Systems Based on a Dual Active Bridge Converter. *Sustainability* **2021**, *13*, 7689. [[CrossRef](#)]
14. Hou, N.; Song, W.; Wu, M. Minimum-Current-Stress Scheme of Dual Active Bridge DC-DC Converter with Unified-phase-shift Control. *IEEE Trans. Power Electron.* **2016**, *31*, 1. [[CrossRef](#)]
15. Najdek, K.; Nalepa, R. The Frequency-and the Time-Domain Design of a Dual Active Bridge Converter Output Voltage Regulator Based on the D-Decomposition Technique. *IEEE Access* **2021**, *9*, 71388–71405. [[CrossRef](#)]
16. Zhou, L.; Gao, Y.; Ma, H.; Krein, P.T. Wide-Load Range Multiobjective Efficiency Optimization Produces Closed-Form Control Solutions for Dual Active Bridge Converter. *IEEE Trans. Power Electron.* **2021**, *36*, 8612–8616. [[CrossRef](#)]

17. Sebastian, E.; Montijano, E.; Oyarbide, E.; Bernal, C.; Galvez-Anguas, R. Nonlinear Implementable Control of a Dual Active Bridge Series Resonant Converter. *IEEE Trans. Ind. Electron.* **2021**, *69*, 1. [[CrossRef](#)]
18. George, K. Design and Control of a Bidirectional Dual Active Bridge DC-DC Converter to Interface Solar, Battery Storage, and Grid-Tied Inverters. Bachelor's Thesis, University of Arkansas, Fayetteville, AR, USA, 2015. [[CrossRef](#)]
19. Ramakrishnan, H. *Bi-Directional, Dual Active Bridge Reference Design for Level 3 Electric Vehicle Charging Stations*; Texas Instruments: Dallas, TX, USA, 2019; pp. 1–51.
20. Chen, L.; Lin, L.; Shao, S.; Gao, F.; Wang, Z.; Wheeler, P.W.; Dragicevic, T. Moving Discretized Control Set Model-Predictive Control for Dual-Active Bridge with the Triple-Phase Shift. *IEEE Trans. Power Electron.* **2020**, *35*, 8624–8637. [[CrossRef](#)]
21. Hebala, O.M.; Aboushady, A.A.; Ahmed, K.H.; Abdelsalam, I.A. Generic Closed-Loop Controller for Power Regulation in Dual Active Bridge DC-DC Converter With Current Stress Minimization. *IEEE Trans. Ind. Electron.* **2019**, *66*, 4468–4478. [[CrossRef](#)]
22. Hebala, O.M.; Aboushady, A.A.; Ahmed, K.H.; Burgess, S.; Prabhu, R. Generalized Small-Signal Modelling of Dual Active Bridge DC/DC Converter. In Proceedings of the 7th International Conference on Renewable Energy Research and Applications (ICRERA), Paris, France, 14–17 October 2018; pp. 914–919.
23. Bindi, M.; Garcia, C.I.; Corti, F.; Piccirilli, M.C.; Luchetta, A.; Grasso, F.; Manetti, S. Comparison Between PI and Neural Network Controller for Dual Active Bridge Converter. In Proceedings of the 2021 IEEE 15th International Conference on Compatibility, Power Electronics and Power Engineering (CPE-POWERENG), Florence, Italy, 14–16 July 2021; pp. 1–6.
24. Hung, V.M.; Stamatescu, I.; Dragana, C.; Paraschiv, N. Comparison of model reference adaptive control and cascade PID control for ASTank2. In Proceedings of the 9th IEEE International Conference on Intelligent Data Acquisition and Advanced Computing Systems: Technology and Applications (IDAACS), Bucharest, Romania, 21–23 September 2017; Volume 2, pp. 1137–1143. [[CrossRef](#)]
25. Van Hoek, H.; Jacobs, K.; De Doncker, R.W. Performance analysis of an analytical calculation tool for dual-active-bridge converters. In Proceedings of the IEEE 11th International Conference on Power Electronics and Drive Systems, Sydney, NSW, Australia, 9–12 June 2015; pp. 1130–1137. [[CrossRef](#)]
26. Fiaz, M.F.; Calligaro, S.; Petrella, R. Analytical Modelling and Control of Dual Active Bridge Converter Considering all Phase-Shifts. In Proceedings of the 2020 IEEE Energy Conversion Congress and Exposition (ECCE), Detroit, MI, USA, 11–15 October 2020; pp. 5984–5991. [[CrossRef](#)]
27. Zhang, Z.; Andersen, M.A.E. High frequency AC inductor analysis and design for dual active bridge (DAB) converters. In Proceedings of the 2016 IEEE Applied Power Electronics Conference and Exposition (APEC), Long Beach, CA, USA, 20–24 March 2016; pp. 1090–1095.
28. Xu, J.; Wang, Y.; Li, K.; Hu, X.; Yin, S.; Li, R.; Lv, C. Fast Transient Current Control for Dual-Active-Bridge DC-DC Converters with Triple-Phase-Shift. In Proceedings of the 2019 IEEE Applied Power Electronics Conference and Exposition (APEC), Anaheim, CA, USA, 17–21 March 2019; IEEE; pp. 2197–2201.
29. Shah, S.S.; Iyer, V.M.; Bhattacharya, S. Exact Solution of ZVS Boundaries and AC-Port Currents in Dual Active Bridge Type DC-DC Converters. *IEEE Trans. Power Electron.* **2019**, *34*, 5043–5047. [[CrossRef](#)]
30. Steub, V. Study of Modulation Schemes for the Dual-Active-Bridge Converter in a Grid-Connected Photovoltaic Park. Master's Thesis, Chalmers University of Technology, Gothenburg, Sweden, 2018.
31. Wang, W.; Zhou, L.; Eull, M.; Preindl, M. Comparison of Litz Wire and PCB Inductor Designs for Bidirectional Transformerless EV Charger with High Efficiency. In Proceedings of the 2021 IEEE Transportation Electrification Conference & Expo (ITEC), Chicago, IL, USA, 21–25 June 2021; pp. 339–346.
32. Xue, L.; Diaz, D.; Shen, Z.; Luo, F.; Mattavelli, P.; Boroyevich, D. Dual active bridge based battery charger for plug-in hybrid electric vehicle with charging current containing low frequency ripple. *IEEE Trans. Power Electron.* **2015**, *30*, 7299–7307. [[CrossRef](#)]
33. Luchetta, A.; Manetti, S.; Piccirilli, M.C.; Reatti, A.; Kazimierczuk, M.K. Comparison of DCM operated PWM DC-DC converter modelling methods including the effects of parasitic components on duty ratio constraint. In Proceedings of the IEEE 15th International Conference on Environment and Electrical Engineering (EEEIC), Rome, Italy, 10–13 June 2015; pp. 766–771.
34. Liu, Y.-F.; Sen, P.C. A general unified large signal model for current programmed DC-to-DC converters. *IEEE Trans. Power Electron.* **1994**, *9*, 414–424. [[CrossRef](#)]
35. Zhu, G.; Luo, S.; Iannello, C.; Batarseh, I. Modeling of conduction losses in PWM converters operating in discontinuous conduction mode. *Proc. IEEE Int. Symp. Circuits Syst.* **2002**, *3*, 511–514.
36. Reatti, A.; Corti, F.; Tesi, A.; Torlai, A.; Kazimierczuk, M.K. Effect of Parasitic Components on Dynamic Performance of Power Stages of DC-DC PWM Buck and Boost Converters in CCM. In Proceedings of the 2019 IEEE International Symposium on Circuits and Systems (ISCAS), Sapporo, Japan, 26–29 May 2019; pp. 1–5.
37. Zhao, B.; Song, Q.; Liu, W.; Sun, Y. Dead-Time Effect of the High-Frequency Isolated Bidirectional Full-Bridge DC-DC Converter: Comprehensive Theoretical Analysis and Experimental Verification. *IEEE Trans. Power Electron.* **2014**, *29*, 1667–1680. [[CrossRef](#)]
38. Shi, H.; Wen, H.; Hu, Y. Deadband Effect and Accurate ZVS Boundaries of Ga, N-Based Dual-Active-Bridge Converters With Multiple-Phase-Shift Control. *IEEE Trans. Power Electron.* **2020**, *35*, 9886–9903. [[CrossRef](#)]
39. Aghabali, I.; Dorn-Gomba, L.; Malysz, P.; Emadi, A. Parasitic Resistance Effect on Dual Active Bridge Converter. In Proceedings of the IECON 2019—45th Annual Conference of the IEEE Industrial Electronics Society, Lisbon, Portugal, 14–17 October 2019; Volume 1, pp. 1932–1937.

40. Krismer, F.; Kolar, J.W. Accurate Power Loss Model Derivation of a High-Current Dual Active Bridge Converter for an Automotive Application. *IEEE Trans. Ind. Electron.* **2009**, *57*, 881–891. [[CrossRef](#)]
41. Zumel, P.; Ortega, L.D.; Fernandez, C.; Rodriguez, R.; Barrado, A. Discrete Model of Dual Active Bridge Series Resonant Converter. In Proceedings of the 20th Workshop on Control and Modeling for Power Electronics (COMPEL), Toronto, ON, Canada, 17–20 June 2019; pp. 1–7.
42. Daneshpajoo, H.; Bakhshai, A.; Jain, P. Modified dual active bridge bidirectional DC-DC converter with optimal efficiency. In Proceedings of the 2012 Twenty-Seventh Annual IEEE Applied Power Electronics Conference and Exposition (APEC), Orlando, FL, USA, 5–9 February 2012; pp. 1348–1354.
43. Cúnico, L.M.; Alves, Z.M.; Kirsten, A.L. Efficiency-Optimized Modulation Scheme for DC—DC Converter. *IEEE Trans. Ind. Electron.* **2021**, *68*, 5955–5965. [[CrossRef](#)]
44. Oggier, G.G.; García, G.; Oliva, A.R. Modulation strategy to operate the dual active bridge DC-DC converter under soft switching in the whole operating range. *IEEE Trans. Power Electron.* **2011**, *26*, 1228–1236. [[CrossRef](#)]
45. Beldjajev, V.; Roasto, I.; Zakis, J. Impact of component losses on the efficiency of a new quasi-z-source-based dual active bridge. *IFIP Adv. Inf. Commun. Technol.* **2013**, *394*, 485–492. [[CrossRef](#)]
46. Song, C.; Chen, A.; Pan, Y.; Du, C.; Zhang, C. Modeling and Optimization of Dual Active Bridge DC-DC Converter with Dead-Time Effect under Triple-Phase-Shift Control. *Energies* **2019**, *12*, 973. [[CrossRef](#)]
47. Wang, D.; Peng, F.; Ye, J.; Yang, Y.; Emadi, A. Dead-time effect analysis of a three-phase dual-active bridge DC/DC converter. *IET Power Electron.* **2018**, *11*, 984–994. [[CrossRef](#)]